DEGREE PROJECT IN PHYSICS,
SECOND CYCLE, 30 CREDITS
STOCKHOLM, SWEDEN 2023

Effect of Proton Irradiation on the Mechanical Properties of Fe-10Cr-4Al in Liquid Lead

SH204X Master Thesis Report

Gabriela Lapinska

KTH ROYAL INSTITUTE OF TECHNOLOGY
NUCLEAR ENERGY ENGINEERING
TRITA-SCI-GRU 2023:038

Authors

Gabriela Lapinska <lapinska@kth.se>
Nuclear Energy Engineering
KTH Royal Institute of Technology

Place for Project

Stockholm, Sweden
Nuclear Engineering
Department of Physics
KTH Royal Institute of Technology

Examiner

Janne Wallenius
Nuclear Engineering
KTH Royal Institute of Technology

Supervisors

Pär Olsson and Faris Sweidan

Nuclear Engineering

KTH Royal Institute of Technology

Abstract

Among the structural materials under consideration for future lead-cooled fast reactors, special attention is paid to ferritic Fe-10Cr-4Al due to its superior corrosion and erosion protective properties, as well as its insensitivity to liquid metal embrittlement in liquid lead. This thesis gives an inside look into the radiation damage properties of the alloy and the possible embrittlement scenarios. The samples were irradiated with 5.5 MeV protons and then tested with a slow strain rate testing rig at 375^{o}C and 450^{o}C. The results showed that for Fe-10Cr-4Al irradiated to a peak dose of 0.14 dpa, the total elongation to failure was reduced by 3-5%, compared to the unirradiated samples. Moreover, the mechanical properties (yield strength, ultimate tensile strength, and fracture elongation) of the irradiated samples depend strongly on temperature. The scanning electron microscopy images show no signs of liquid metal embrittlement. However, the brittle structures at the edges of the samples could indicate the existence of hydrogen embrittlement.

Keywords

Fe-10Cr-4Al, Lead, Radiation Damage, Slow Strain Rate Testing

Abstract

Bland de strukturmaterial som övervägs för framtida blykylda snabba reaktorer (LFR) ägnas särskild uppmärksamhet åt ferritiska Fe-10Cr-4Al-legeringar på grund av deras överlägsna korrosionsbeständighet och deras avsaknad av försprödning i den flytande blymiljön. Denna avhandling ger en inblick i legeringens strålskador och möjliga försprödningsscenarier. Proverna bestrålades med 5.5 MeV protoner och testades sedan med SSRT-testriggen vid 375^{o}C och 450^{o}C. Resultaten visade att för prover av Fe-10Cr-4Al bestrålat till en dos av 0.14 dpa, minskade den totala förlängningen till brott med 3-5%, jämfört med de obestrålade proverna. Dessutom uppvisar de mekaniska egenskaperna (YS, UTS och brottförlängning) hos de bestrålade proverna en större temperaturinverkan. Bilder tagna med svepelektronmikroskopi (SEM) visade inga tecken på flytande metallförsprödning (LME). De spröda strukturerna vid kanterna av proverna, där protonerna implanterades, kan dock indikera förekomsten av väteförsprödning.

Acknowledgements

I would like to express my sincere gratitude to my supervisors, Pär Olsson and Faris Sweidan, for their invaluable guidance and support throughout this project. I am particularly grateful to Faris for always ensuring that I never felt confused or lost during the process and for creating an environment where I felt comfortable asking any question. I deeply appreciate all the assistance and knowledge shared by Pär. Despite not being able to reference his gut feeling, the brainstorming meetings were immensely helpful in shaping the thesis.

When I started this project, my understanding of material damage was limited. Therefore, I am immensely grateful for Christopher Petersson's patience and assistance, which were invaluable in enhancing my knowledge in this area. Moreover, none of this would have been possible without Gyula Nagy's dedication to the radiation process, the most time-consuming part of the project.

Lastly, I would like to extend my heartfelt thanks to all my friends and family for their constant support throughout this journey. Regardless of how stressed or distracted I may have been, it has been truly invaluable.

Acronyms

HE	Hydrogen Embrittlement
HEDE	Hydrogen-Enhanced Decohesion
HELP	Hydrogen-Enhanced Localized Plasticity
FeCrAl	Iron-Chromium-Aluminium
LFR	Lead-cooled Fast Reactor
LME	Liquid Metal Embrittlement
LWR	Light Water Reactor
NPP	Nuclear Power Plant
PWR	Pressurized Water Reactor
RE	Reactive Element
SEM	Scanning Electron Microscope
SSRT	Slow Strain Rate Testing
UTS	Ultimate Tensile Strength
YS	Yield Strength

Contents

Chapter 1

Introduction

1.1 Aim

With a new generation of nuclear reactors anticipated to operate at elevated temperatures and radiation doses, the challenge of selecting reliable structural materials arises. The superior corrosion resistance in comparison to numerous other commonly used materials and good ductility properties of FeCrAl alloys in liquid lead (Pb) make them very promising materials to be used in lead-cooled fast reactors (LFR). The main aim of this thesis is to investigate and characterize the surface irradiation effects on Fe-10Cr-4Al after irradiation with 5.5 MeV protons. The Fe-10Cr-4Al alloy has recently been shown to not be susceptible to liquid metal embrittlement (LME) in liquid lead, all the while it shows typical ferritic susceptibility to LME in lead-bismuth eutectic (LBE). The alloy is proposed as a corrosion and erosion protective overlay material that can be added to e.g. cladding tubes in LFR designs, and it is thus of importance to determine if the good mechanical and chemical properties are maintained under irradiation as well. Radiation can cause hardening and a decrease in ductility in itself, but may also make the material susceptible to LME due to the build up of radiation damage. Susceptibility to LME can be determined using tensile experiments performed with a slow strain rate testing (SSRT) rig. Further investigation using scanning electron microscopy (SEM) should give more insight into the origin of the ductility decrease. The possible scenarios include embrittlement caused by the radiation damage buildup, liquid metal embrittlement, or the high concentration of hydrogen implanted into the samples.

1.2 Environmental aspects

The increasing demand for electricity due to the growing world population and drive towards prosperity has created a need for reliable access to energy supply. Generating electricity through the utilization of fossil fuels has a negative impact on both humans and the environment, resulting in substantial amounts of greenhouse gas emissions that contribute to climate change and further pollution of the air, water, and soil. Thus, it is crucial to transition to clean technologies to address the issue. If the current rate of increase in global warming continues, it is expected that the temperature will rise to 1.5°C sometime between 2030 and 2052 [1]. According to the Intergovernmental Panel on Climate Change (IPCC's) estimations, in order to mitigate the most severe consequences of climate change, it is necessary to decrease emissions by approximately 45% before the year 2030 and achieve a state of net-zero emissions by the year 2050.

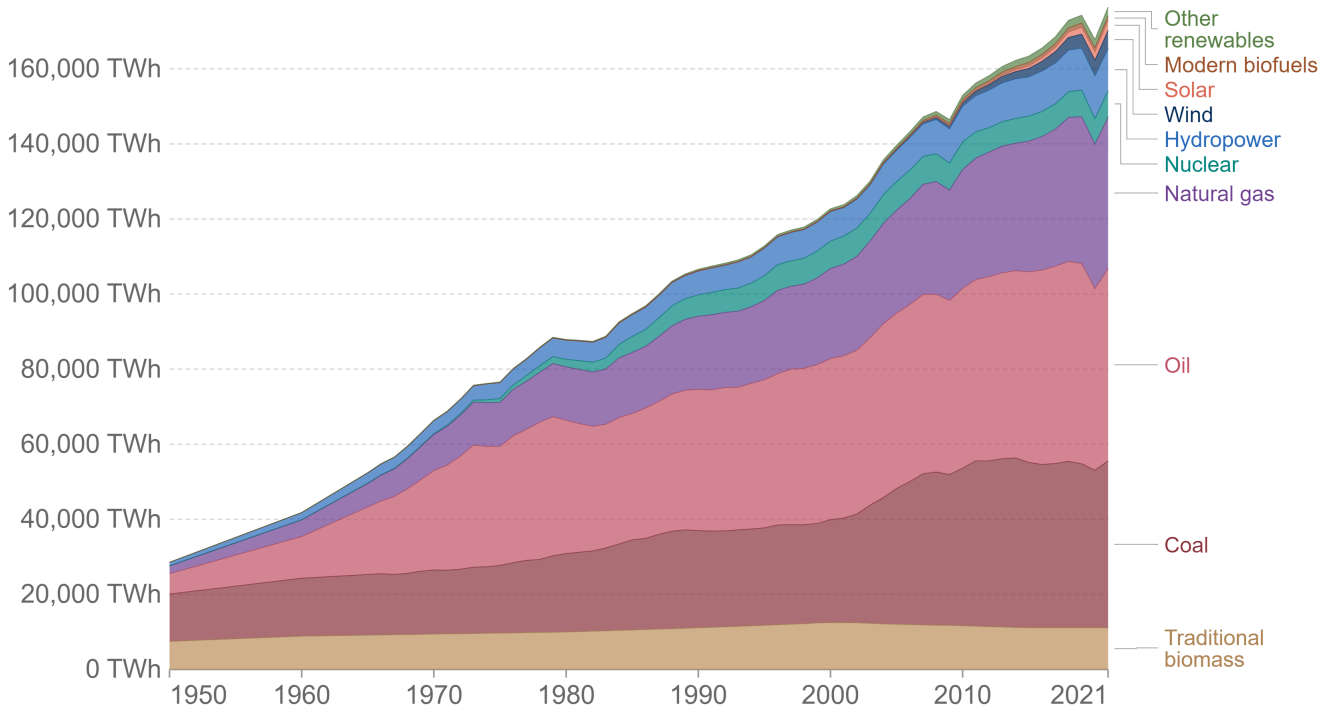

Figure 1.2.1: Global energy consumption by source [2].

Figure 1.2.1 shows the energy mix with a diverse range of sources – coal, oil, natural gas, nuclear, hydropower, wind, solar, and biofuels. Globally, the largest amount of energy comes from oil, followed by coal and gas. Thus, the energy mix is dominated by fossil fuels accounting for over 80% of the energy consumption. It was not until the 1960s that nuclear energy was added to the mix.

Nuclear energy offers significant amounts of reliable and reasonably priced energy that is much more environmentally friendly than fossil sources, as the nuclear power plants can function uninterrupted for an extended period of time, regardless of weather conditions. The governments reaffirmed their commitments to reducing greenhouse gas emissions at the 26^{th} United Nations Climate Change Conference (COP26) in Glasgow, where 65 countries declared to accelerate the phase-out of coal. However, the economic recovery from COVID-19 has led to an increase in energy demand that exceeds the growth of clean energy production and involves a greater reliance on fossil fuels. Energy prices are rising and the conflict in Ukraine also highlights the vulnerability of the fossil fuel supply chain even more due to issues with gas import. In order to follow the energy demand, unsustainable solutions have been applied such as restoring coal-fired power plants. Thus, many governments recognise the need for more long-term and secure solutions with nuclear energy being considered as an important player on the way to net-zero emissions.

1.3 Nuclear energy

In 2021, nuclear reactors produced 2653 TWh in total with electricity-generating reactors marking the highest total capacity (370 GWe) in a single year thus far [3]. This shows the upward trend since a drop in 2012 after the Fukushima accident which influenced negatively the public confidence in nuclear energy. However, the nuclear reactor fleet decreased from 441 to 436, compared to the year 2020. Pressurized water reactors (PWRs) make up around 70% of all operational reactors and they are the most favoured type of reactors being built in the last 5 years. The number of units under construction increased by four in comparison with 2020 and it was 53 at the end of 2021.

The increasing interest in nuclear power plants shows that countries, experts, and members of society recognise the crucial role of nuclear energy in combating climate change. Public acceptance continues to rise, with a record-high percentage of the public favouring nuclear energy. In 2022, the National Nuclear Energy Public Opinion Survey found that 77% of respondents are strongly or somewhat in favour of using nuclear energy as the source of electricity in the United States, compared to around 60% in the previous decade [4]. In Sweden, an opinion poll by Novus showed a similar uprising trend for respondents in favour of building new reactors if necessary, from

46% in November 2021 to 56% at the end of March 2022. The willingness to continue with nuclear energy is at 84% and only 10% of respondents want to close reactors through political decisions [5].

The accidents that caused distrust in nuclear power, such as Unit 2 of Three Mile Island NPP (1979), Chernobyl (1986), and Fukushima (2011), lead to extensive research to enhance the safe operation of reactors. Currently, the industry is continuously enhancing safety analysis and adopting a defense-in-depth approach, which entails the integration of independent layers of protection. Careful design with multiple physical barriers, such as the fuel matrix, the fuel cladding, the boundary of the reactor coolant system and the containment system, aims at preventing accidents and ensures protection in the event that accident prevention fails. Any potential detrimental effects on society or the environment can take place only after all the protective measures undergo failure. The design of new-generation reactors utilizes passive safety systems that are inherently safer than the old systems used in, for example, Fukushima, where the accident could have been prevented with the use of passive safety.

Despite being perceived as a high risk industry, nuclear power causes much fewer deaths when compared to other energy sources. The most deaths are assigned to the Chernobyl accident where estimated 4000 people lost their lives due to radiation exposure [6]. However, the death rates that are measured based on the casualties from the accidents and air pollution are significantly higher for coal, oil, biomass, gas and hydropower. Figure 1.3.1 shows the difference of a few orders of magnitude between the most dangerous brown coal (32.72) and nuclear energy (0.03).

1.4 Generation-IV reactors

In 2001, the Generation IV International Forum (GIF) was established to discuss collaboration in the development of new nuclear systems that could be commercially deployable by 2030. They also defined a number of goals that Generation-IV (Gen-IV) systems should meet. In terms of sustainability, clean air and long-term system availability, the objectives have been satisfied by effectively utilizing fuel and minimizing nuclear waste leading to a significantly lesser impact on the environment. It means that there should be at least breeder reactors that increase fuel resources by nearly a factor of 100 by breeding fissile fuel from ^{238}U or ^{232}Th [8]. Designs of Gen-IV fast reactors, that use fast neutrons instead of the slow neutrons produced

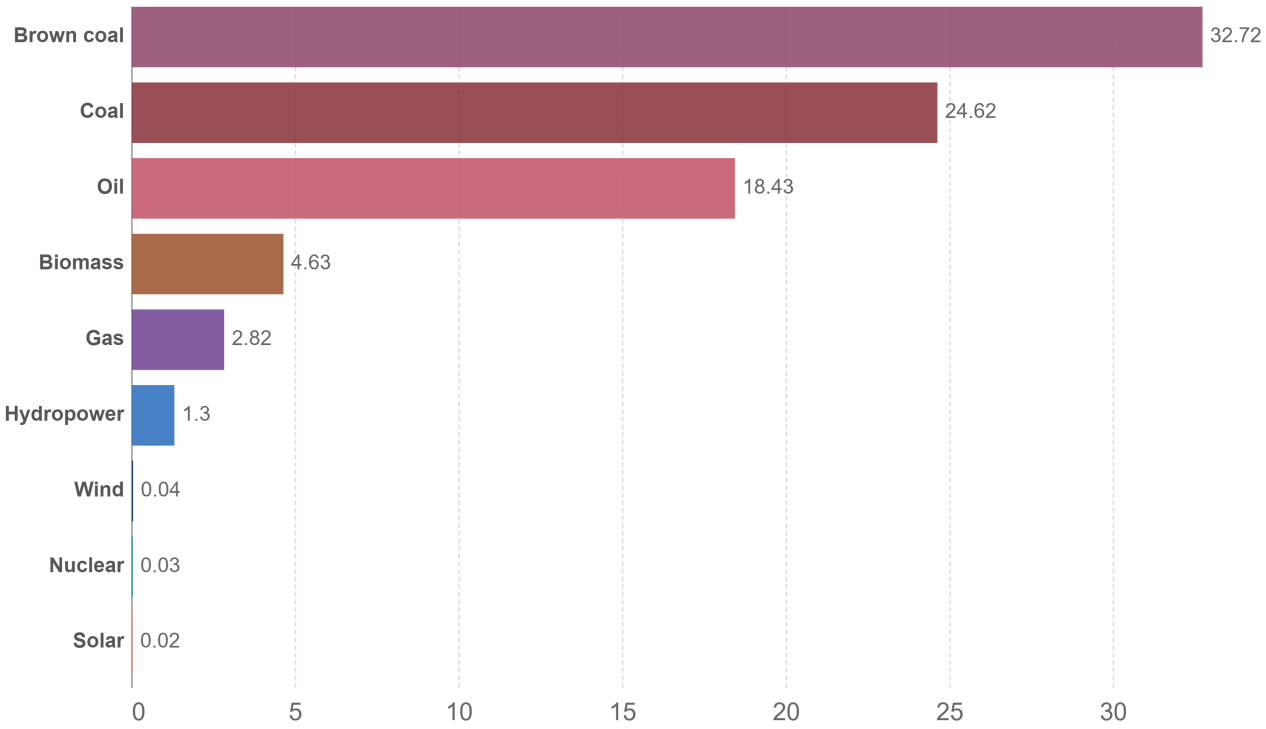

Figure 1.3.1: Death rates per unit of electricity production [7].

by conventional reactors, aim to recycle not only bred ^{239}Pu but also minor actinides created in the fuel by nuclear transmutation. The process reduces the radiotoxic inventory for the final waste disposal. New reactors are expected to enhance safety and reliability by minimizing the likelihood of core damage and eliminating the need for off-site emergency response. For the economical part, the aim is a financially favourable life-cycle as compared to other energy sources, as well as an investment risk that is not higher than the alternatives. The last objective is the proliferation resistance and protection against diversion or weapon-usable materials [9].

The six reactor technologies that were chosen for further research include the Sodium-cooled Fast Reactor (SFR), Lead-cooled Fast Reactor (LFR), Gas-cooled Fast Reactor (GFR), Very High Temperature Reactor (VHTR), Molten Salt Reactor (MSR), and Supercritical Water-cooled Reactor (SCWR). There is a total of 390 reactor-years of operational experience with NaK and ^{23} Na-cooled reactors over five decades in eight countries with two reactors producing power on a commercial basis (BN-600 and BN-800, Russia) [10]. Furthermore, there is a broad range of experience in the operation of He-cooled HTRs and some with molten salt reactors, which have been successfully implemented in various locations worldwide. However, the upcoming years will bring more expertise with new reactors under construction, such as BREST-300 the first new

generation LFR, and new designs being constantly studied.

1.5 Lead-cooled fast reactors

The LFR is an advanced Gen-IV reactor that meets the objectives set by GIF and is one of the most promising among the six types of reactors. By operating with a fast neutron spectrum and employing a closed fuel cycle, this system demonstrates the capacity to efficiently utilize depleted uranium fuel matrices and burn the actinides from spent LWR fuel. Thus, it offers substantial potential in proliferation resistance and economic performance. Taking into consideration the abundance of lead as a material, its availability does not present any significant challenges, even when considering the construction of a substantial number of LFRs. Thus, molten lead is considered a sustainable coolant. The safety has been improved by using molten lead or lead-bismuth eutectic coolant at atmospheric pressure. The loss-of-coolant accidents can be eliminated by using a guard vessel that is properly designed [11]. Moreover, it adds simplicity to plant design as there is no need to simultaneously control temperature, pressure, and coolant level. The very high boiling temperature of lead (1749 ^{o}C) eliminates the coolant boiling concerns and enhances the inherent safety. Lead coolants are relatively inert, thus there are no rapid chemical reactions between lead coolants and water/air. It reduces the risk of energy release in accident conditions, such as the hydrogen explosions at the Fukushima reactors. The LFRs are designed with enhanced passive safety by enabling fuel cooling by natural circulation. The thermodynamic characteristics of lead, along with its simple coolant flow paths and minimal core pressure loss, enable the primary decay heat removal system to achieve an exceptionally high degree of natural circulation cooling. It does not require backup power and is resilient to blackout conditions if appropriately designed, the situation that was a primary problem in the Fukushima accident.

The challenges that LFRs face are associated with the high melting point (327 ^{o}C) of lead, its opacity, and its susceptibility to drive corrosion of structural materials. The former requires the primary coolant system to be maintained at high enough temperatures to avoid the solidification of lead or, at the very least, support a recirculation at the core level [11]. However, the high-temperature requirement for cold shutdown during maintenance poses challenges for inspections and fuel handling due to the opacity of lead. This issue could be addressed by performing remote

maintenance operations or ultrasonic inspections [12].

Since LFRs operate in new conditions with liquid lead coolant, the problem of selecting structural materials arises, since the materials used in currently operating conventional reactors are not suitable for use in such severe operation conditions. Thus, this work primarily focused on investigating one of the proposed structural materials for future LFRs. Testing under irradiation and high temperatures is necessary in search of reliable materials for reactor use.

Chapter 2

Theoretical Background

2.1 Alumina-forming steels

It is widely recognized that steels are susceptible to corrosion from liquid lead (Pb) when exposed to high temperatures [13], thereby restricting the maximum operating temperature of lead-cooled fast reactors (LFRs). The ferritic stainless steels possess several advantages, including cost-effectiveness and high availability. These steels are commonly alloyed with a significant amount of chromium, which facilitates the formation of a protective chromia (Cr_2O_3) scale. However, chromia scale is less effective compared to the superior corrosion-resistance properties of alumina (Al_2O_3) forming steels [14]. To address problems with oxidation and corrosion, the implementation of FeCrAl alloys with self-healing alumina-forming properties has been suggested.

2.1.1 FeCrAl

The benefits arising from the use of FeCrAl alloys go beyond the high-temperature oxidation resistance that extends the coping time (the time during which mitigation actions are taken to ensure that the temperature of the cladding remains below its creep rupture or melting point) and limits the hydrogen generation under design basis and severe accident conditions. They also involve stress corrosion cracking and inherent corrosion resistance, as well as a reduction in radiation-induced swelling, when compared to nuclear-grade zirconium-based alloys or austenitic stainless steels [15].

Commonly used chromia forming austenitic stainless steels, such as 316L, show poor corrosion resistance in liquid lead at temperatures above 500^{o}C as it experiences difficulties in forming protective oxides [13]. Chromia forming 316L showed lead penetration at a depth of roughly 100–300 μm, while alumina (Al_2O_3) forming 14Ni AFA was the only alloy in the test that was not affected from any dissolution attack by the liquid lead.

Above 550^{o}C lead becomes severely corrosive, thus alumina-forming alloys, such as ferritic FeCrAl steels, with superior oxidation behaviour are investigated for use in significantly higher temperatures to improve the normal operation corrosion performance.

The comparative study at KTH showed the corrosion effect on different commercially used FeCrAl steels with varying chemical compositions. In conclusion, Fe-10Cr-4Al-RE alloy (also denoted as 10-4, now sold as Kanthal 100 EF) performed considerably better in liquid lead at 800^{o}C and 900^{o}C, compared to Kanthal APM^{TM} and Kanthal APMT^{TM} steels [16]. A protective alumina scale was formed on the surface of 10-4 with no sign of corrosion attacks at 800^{o}C. At 900^{o}C, there were no signs of dissolution or lead penetration. However, 10-4 suffered from internal oxidation up to 500 μm depth. The other FeCrAl steels showed internal oxidation already at 800^{o}C and little to no protective oxide scale visible on the surface at 900^{o}C [16].

The composition in wt%, as well as different Reactive Elements (RE) additions, affect the properties of FeCrAl steels. The superior oxidation performance of FeCrAl alloys is related to the preferential oxidation of Al inside the alloy, which results in the formation of a protective alumina layer on the exposed surface. Moreover, if enough Cr and Al are present in the alloy, alumina production is promoted [15]. The focus on creating alloys that display the usual oxidation resistance of the higher Cr FeCrAl alloys but have much lower Cr concentration is a result of the radiation embrittlement process for FeCrAl alloys. It is projected that more Al will be required in order to compensate for the shortage of Cr [15]. However, higher Al content lowers the fabricability of the alloy as it has a detrimental effect on ductility. The alloy's capability to be hot- or cold-worked into its final shape decreases as the Cr and/or Al content increases[15].

FeCrAl alloys typically contain a portion of RE additives (less than 1 wt%), such as Ti, Nb, Zr, Y, and Hf. Using a precipitate hardening mechanism, FeCrAl alloys become stronger and less ductile with the addition of Nb and Ti [15]. The long-term oxidation

studies show that the RE are essential for the growth of thin and even protective oxides that increase the lifetime of structural components [17].

2.2 Radiation Damage

Radiation damage has significant importance in the studies of structural components within or near the core of the nuclear reactor. The materials must sustain extreme conditions of high temperature, high pressure, and corrosive environment as well as irradiation that induces specific forms of damage [18]. It disturbs the microstructure of the material by forming defects, including dislocation loops, precipitates, grain boundary segregation, cavities, and bubbles. In consequence, the radiation damage gives rise to phenomena such as radiation hardening and embrittlement.

Radiation damage occurs when the incident radiation possesses sufficient energy to displace atoms from their equilibrium positions within the crystal structure. This displacement results in the formation of vacancies (atoms missing in the lattice site) and self-interstitials (crystal atoms crowded or in spaces that should be not normally be occupied in the lattice). The atom that is initially struck and displaced is commonly referred to as the primary knock-on atom (PKA). If the energy of a PKA is sufficiently high, it has the potential to create additional knock-on atoms. These secondary knock-on atoms, also known as recoils, initiate a cascade of displacements throughout the material. This cascade continues until the energy of the atoms involved is no longer sufficient to generate further knock-on atoms. At that point, the damage event comes to a halt. Notably, this phenomenon can be observed not only under neutron irradiation but also when electrons and ions are incident upon the material. In fact, studies simulating neutron-induced radiation damage have frequently employed electrons and ions as surrogate species.

2.2.1 Proton irradiation to simulate the neutron damage

Neutron irradiation experiments require specialized facilities and special sample handling procedures since they always activate the samples to some extent. Moreover, the long cycle length (exposure time) impacts the high cost of such irradiation. In contrast, ion irradiation offers several advantages in terms of prolonged irradiation time, activation, and cost. It generates minimal or negligible residual radioactivity,

enabling handling of samples without extensive precautions. For a few MeV, the penetration depth typically extends beyond 40 μm, offering sufficient depth of penetration to allow for the assessment of properties such as irradiation hardening [19].

Due to their inherent electrical neutrality, neutrons can penetrate extensive distances, resulting in a damage profile that remains spatially flat over several millimeters of material. The importance of protons in emulation of neutron irradiation effect relates to the relatively flat damage profile, resulting in a dose rate variation of less than a factor of 2 across several tens of m. However, at the end of the proton path, it deposits most of the energy, that takes a form of a Bragg peak (depicted on the Fe-10Cr-4Al damage profile in Figure 3.3.3).

While the mechanism of damage may differ between neutron and proton irradiation, numerous studies have demonstrated that high-energy proton beams can effectively emulate the effects of neutron irradiation under certain conditions [20–22]. There is a growing amount of evidence supporting the use of proton irradiation. The studies consistently demonstrate that resulting microstructural features (such as dislocation loops, precipitates, voids and radiation-induced segregation) align well with those observed in materials subjected to reactor radiation [21]. In proton-irradiated Zircaloy-4, the observed microstructures were in agreement with neutron-irradiated samples [22]. Moreover, the properties assessed, including hardness, exhibit excellent agreement with their reactor-irradiated counterparts. The magnitude of hardening and the dose dependence were very similar for neutron and proton irradiation [20]. Both irradiation methods exhibited nearly identical increases in yield strength, as determined through hardness measurements and microstructure analysis. However, there can be a substantial chemical effect from proton irradiation due to the hydrogen implantation. Therefore self-ion irradiation is often the preferred method, but at the cost of very limited penetration depth.

2.2.2 Radiation Hardening

When metals and alloys are exposed to energetic irradiation, Frenkel pairs are generated, consisting of self-interstitials and vacancies. The interstitial atoms are very mobile relative to the vacancies, enabling them to combine and form dislocation loops. Given sufficient time and a high enough temperature, the vacancies that do

not recombine with interstitials form into voids. The process of irradiation hardening occurs due to the formation of a high density of dislocation loops and/or voids and tangles caused by displacement damage, sometimes coupled with precipitate changes induced by irradiation. These phenomena lead to a noticeable enhancement in the yield stress and ultimate tensile strength, often connected to a corresponding reduction in ductility. While this hardening effect is observed in all metals and alloys, it holds particular significance for body-centered-cubic materials like ferritic steels and FeCrAl. Apart from the decrease in ductility accompanying the increase in strength in these steels, the hardening process also impacts their toughness.

The impact of irradiation on the tensile behaviour is temperature-dependent. Below temperatures of 425-450^{o}C, irradiation results in the hardening of the steels. On the other hand, when irradiation occurs above this temperature range, the properties generally remain unchanged, although there might be some enhanced softening depending on the fluence [23]. The increased rate of softening is the consequence of the enhanced diffusion and redistribution of precipitates, which accelerate the recovery and coarsening mechanisms. This is due to the elevated temperatures causing gradual changes in the microstructure through dislocation recovery processes and precipitate coarsening.

At temperatures below 400^{o}C, irradiation hardening demonstrates an upward trend with an increasing dose for ferritic–martensitic steels. The yield stress or hardness of irradiated materials typically shows an increase with the irradiation dose until the density of irradiation-induced defects reaches a saturation point when compared to their unirradiated counterparts. No saturation of yield strength has been observed up to a dose of 10 dpa [24].

2.3 Embrittlement

The Fe-10Cr-4Al samples are expected to experience a reduction in ductile behaviour and there are several possible phenomena that can account for premature fracture. The proposed explanations for the irradiated sample behaviour after tensile testing involve radiation damage, hydrogen effect, and liquid metal embrittlement (LME).

2.3.1 Radiation Embrittlement

In metals, exposure to radiation can lead to radiation hardening, as described above. This generally strengthens the material but also makes it more susceptible to embrittlement, which is characterised by reduced toughness and ductility, as well as an increased likelihood of brittle fracture. This occurs due to the displacement of atoms from their lattice sites through the initial interaction with radiation and the subsequent cascade of damage (refer to Section 2.2 for more details).

The occurrence of irradiation embrittlement is driven by similar factors to those that cause radiation hardening, such as the formation of defect clusters, dislocations, voids, and precipitates. Throughout the plastic deformation process, the continuous interaction between dislocations and these radiation-induced defects leads to the formation of additional irradiation-induced defects and dislocations that are accountable for the occurrence of irradiation embrittlement [25]. Due to variations in these parameters, accurately predicting the extent of embrittlement becomes challenging.

2.3.2 Hydrogen Embrittlement

Hydrogen embrittlement (HE) is a process resulting in degradation and premature failure of the material by a decrease of ductility due to the presence of atomic hydrogen. According to current knowledge, the hydrogen embrittlement mechanism suggests that hydrogen from the environment infiltrates the steel, dissolving into its structure. These hydrogen atoms then navigate within the steel towards the regions of internal stress concentration, such as crack tips. This migration process facilitates the initiation and propagation of cracks within the steel, ultimately leading to failure. In the case of ferritic steels, excessive hydrogen tends to become trapped within structural defects, which are grain boundaries, dislocation or microvoids [26]. Over time, these trapped hydrogen atoms combine, forming hydrogen gas molecules, which further contribute to the acceleration of fracture through various hydrogen embrittlement mechanisms. For proton-irradiated materials, the hydrogen comes not from the environment but from the irradiation itself.

The extent of embrittlement in ferritic steels is influenced by various factors, including the test conditions and the interaction between hydrogen and the material. The structural composition of ferritic steels plays a crucial role in determining their

mechanical response to hydrogen. Generally, body-centered cubic (bcc) structured ferrite exhibits lower resistance to hydrogen embrittlement compared to face-centered cubic (fcc) structured austenite. This results in a lower solubility of hydrogen in ferritic steels and significantly faster diffusion of hydrogen through the material, by several orders of magnitude [27]. The reduced solubility makes ferritic steels more susceptible to even small amounts of hydrogen in the environment, while the rapid hydrogen motion within the material increases the sensitivity to the effects of microstructural features. Since ferritic steels can have a wide range of microstructures, their susceptibility to hydrogen embrittlement varies significantly.

While it is widely accepted that hydrogen embrittlement occurs due to the accumulation of atomic hydrogen at internal stress centers, the precise micromechanism of failure is not yet fully understood. Different research groups have proposed various mechanisms to explain hydrogen embrittlement. Despite the significant research conducted on the topic, one of the major challenges in addressing hydrogen embrittlement is the lack of complete understanding regarding the underlying mechanism. Two major mechanisms proposed involve hydrogen-enhanced decohesion (HEDE) and hydrogen-enhanced localized plasticity (HELP). However, the phenomenon of hydrogen embrittlement cannot be fully explained by a single micromechanism that applies universally to all materials and operating conditions. The HELP is based on experimental observations that reveal increased dislocation mobility and the presence of well-developed dislocation structures beneath the fracture surface [28]. However, there remains a significant gap in understanding how this locally ductile behaviour eventually transitions to brittle fracture. The HEDE theory postulates that the localized accumulation of hydrogen at crack tips can contribute to the weakening of metal bonds, ultimately leading to fracture [29]. However, it does not provide an explanation for the observed enhancement of plasticity in the material.

The existing literature indicates that in the presence of hydrogen, the fracture of ferritic steels predominantly takes place perpendicular to the direction of the maximum principal tensile stress [30]. A significant characteristic of hydrogen embrittlement is the shift from ductile to brittle fracture behaviour in the presence of hydrogen. In the case of polycrystalline materials, this transition is typically associated with hydrogen-induced fracture occurring at the microscopic level, involving a shift from transgranular fracture to intergranular fracture. Moreover, the fracture surfaces

exhibit distinctive flat surfaces, intergranular facets, voids, and ”quasi-cleavage” features, which resemble cleavage-like patterns but do not align with any established cleavage plane or grain boundaries [31].

2.3.3 Liquid Metal Embrittlement

A significant limitation that is challenging for the deployment of LFRs is the incompatibility between the steels and LBE/liquid Pb at relatively low temperatures. Liquid metal embrittlement (LME) is a phenomenon that can result in premature failure of ferritic steels subject to stress in the LBE/liquid Pb environment. It occurs when molten metals come into contact with a susceptible material that exhibits ductility in ambient conditions. However, the material becomes brittle when exposed to a specific liquid. Heavy liquid metals, such as LBE and Pb, typically induce LME in steels [32]. Consequently, addressing LME becomes crucial to ensure the safety of future liquid metal-cooled reactors.

The complexity of the phenomenon makes it difficult to fully understand and develop models to predict and avoid LME in the design. In order to prevent any significant detrimental impact, numerous variables need to be controlled, such as temperature, grain size or wettability. The grain size is significant as materials with larger grains generally experience more severe embrittlement [33]. Additionally, increased grain size increases the brittle to ductile transition temperature.

The LME is characterised by a reduction in the strain to fracture, when the material is examined in the presence of liquid metal, compared to results obtained in air. This reduction is typically influenced by temperature with LME starting to occur slightly above the melting point of the liquid. When the temperature of the test increases sufficiently, the LME effect disappears, showing a “ductility trough” [32].

The existence of any intervening oxide layer on the solid metal surface prevents LME [33]. Thus, wetting is required to ensure close contact between the two metals. Another prerequisite is plastic deformation, even though LME appears as macroscopically brittle [32]. It significantly reduces ductility. LME impacts the performance of solid material only when it is in direct contact with liquid metal, which means that the alterations to the properties, such as yield strength or ultimate tensile strength (UTS), are not permanent. If the solid sample is removed from the liquid metal environment, the behaviour reverts to the original ductile nature as it performs in the air.

LME transpires through the initiation of a crack at the wetted surface of a solid, followed by propagation into the bulk until the failure occurs. For the comprehensive analysis of the phenomenon, a few issues have to be addressed, such as i) the mechanism of transportation between the atoms of the liquid and solid metal, ii) the transition from ductile to brittle fracture [32, 34]. The differences in approaching these two issues contribute to the variety of models being developed to enhance the understanding of LME.

2.4 Related Work

As FeCrAl is considered to be a candidate structural material in lead-cooled reactors, its compatibility with liquid lead-bismuth eutectic (LBE) and liquid lead (Pb) needs to be studied. The degradation mechanism primarily considered in this work is LME and it has been investigated that steels, especially ferritic steels, are susceptible to LME in LBE and liquid Pb environments [35–37].

More attention was brought to testing Fe-10Cr-4Al in LBE, where it experiences a strong LME effect [36, 38]. The samples tested at 350^{o}C show a substantial reduction in the total elongation to failure, 21.6% in oxygen-saturated and 17.4% in an oxygen-depleted environment. Stronger ductility degradation in the latter indicates the weaker effect of the protective oxide layer on the surface of the sample. It delays LME, while tested in oxygen-saturated conditions.

As mentioned in Section 2.3.3, LME is more important around the melting point and the effect decreases with increasing temperature. There is strong evidence for the existence of ductility trough for Fe-10Cr-4Al tested in LBE [37–39]. The LME effect is most severe at around 350-375 ^{o}C. The sample can experience LME between around 150 ^{o}C up to 450 ^{o}C, after which, it recovers its original ductility. Yield strength and ultimate tensile strength of Fe-10Cr-4Al are not affected by LBE, in comparison to the total elongation to failure which is significantly reduced by LME. LME primarily affects the plasticity at a crack tip, rather than influencing the overall plasticity of the bulk alloy.

For Fe-10Cr-4Al samples tested in lead, the strain at rupture is not influenced by the change in the test temperature [37]. To understand the Fe-10Cr-4Al susceptibility to LME in LBE and liquid Pb, it is important to compare the properties of liquid metals

and their interactions with the alloy. According to the AICRM (Section **??**), together with the requirement for intimate contact between the liquid and solid metal, it implies the existence of some chemical affinity for LME to occur. It is contrary to the statement that embrittlement is typically absent in systems that involve stable intermetallic compounds. It is plausible that this chemical affinity is related to the differences in electronegativity between the metals [40]. However, the observed correlation of electronegativity shows an inverse relationship to its difference between the metals. For simplicity, Fe-10Cr-4Al can be represented by Fe with the electronegativity of 1.83, whereas the values for Pb and Bi are 2.33 and 2.02, respectively. The greater difference in electronegativity occurs between Fe and Pb, which could imply lower susceptibility to LME.

In LBE, oxygen exhibits a higher preference for binding with lead atoms rather than bismuth atoms. Consequently, Pb-O couple tends to be more attracted to the oxide layer on the surface of FeCrAl, compared to bismuth. Promoting absorption of Pb into the oxide layer and subsequently into the alloy allows for LME [41]. Thus, the addition of bismuth to lead increases the sensitivity to LME. In the study conducted on T91 steel, no LME was observed with lead, while the sample was tested in Bi, Pb and LBE at 300^{o}C and 400^{o}C [41]. Among the three liquid metals, LBE showed the highest degree of embrittlement, followed by bismuth and then the least embrittling liquid lead. The former showed a fully brittle fracture surface at 300^{o}C slow strain rate test.

The grain size effect on LME, as mentioned in Section 2.3.3, has been studied with three different FeCrAl alloys, which had chromium-aluminium content of 10-4, 15-4 and 10-6 [42]. The increased susceptibility of Fe-10Cr-6Al alloy to LME can be attributed, in part, to its larger grain size. A structure inherently possesses fewer grain boundaries, which may result in reduced resistance to crack propagation and, consequently, stronger LME susceptibility. It is also recommended to reduce Al content in order to reduce the LME effect of the alloy, as the observations imply that the presence of Al in FeCrAl alloys can increase their susceptibility to LME compared to Cr.

The results of Fe-10Cr-4Al tests show no signs of embrittlement when exposed to liquid lead. This indicates that Fe-10Cr-4Al steel has the potential to be utilized as a construction material in LFRs. However, the effect of the surface irradiation has not been studied.

On materials susceptible to LME, the embrittlement is intensified by irradiation. The T91 samples irradiated with 72 MeV protons up to 0.2 dpa doses and then tensile tested in LBE showed embrittlement, by a significant reduction in the total elongations [43]. Even with such small doses, slight hardening was observed. In another study, the T91 samples irradiated to a slightly higher dose of 0.48 dpa also show an embrittlement effect and was hardened by the irradiation [44].

The slow strain rate tensile testing was conducted in argon and LBE with T91 and F82H steels after irradiation to higher doses [44]. The F82H specimens demonstrate notable irradiation-induced hardening within the temperature range of 150-350^{o}C. The effect of embrittlement is not observed at 150^{o}C, however, it becomes significant at 250^{o}C and 300^{o}C. Interestingly, in the test conducted at 350^{o}C, the sample with an irradiation dose of 19.5 dpa exhibited significant brittleness when tested in LBE and argon.

Furthermore in the study, the stress-strain curve of the 10.9 dpa T91 specimen tested in LBE at 500 °C closely resembles that of the specimen tested in Ar at the same temperature. This indicates that there is no additional embrittlement caused by LBE at temperatures exceeding 450 °C. For lower temperatures of 250^{o}C, 400^{o}C and 450^{o}C, the tests in LBE show a reduced total elongation of up to around 5% compared to tests in argon. The ductility trough is said to be more pronounced and wider compared to the unirradiated T91 samples tested in LBE [44]. Overall, the fracture strain of the irradiated samples can drop to as low as 2-3 %.

The interesting finding regarding irradiated T91 specimens revolves around the consistency in irradiation hardening observed at similar doses, that is comparable for irradiation with solely neutrons and the combination of protons and neutrons [45]. Furthermore, the total elongation shows an increasing linear correlation with increased dose. Thus the irradiation-induced damage is directly related to the detrimental effect of embrittlement.

The presented irradiation studies focus mainly on different ferritic/martensitic steels such as T91. However, there is no evidence for Fe-10Cr-4Al irradiation damage properties. Moreover, LBE is the most often chosen environment for tensile tests with only recent studies showing evidence for no sign of LME in liquid lead. This thesis is designed in a way to fill the gaps and test Fe-10Cr-4Al samples in the liquid lead after proton irradiation.

Chapter 3

Method

3.1 Fe-10Cr-4Al samples

The Fe-10Cr-4Al samples were developed by KTH together with Kanthal [37]. The composition in weight percentage is shown in Table 3.1.1. The mix of titanium, niobium, and zirconium, as reactive elements (RE), was added to provide better oxidation properties by improving the formation of a thin and even more protective oxide layer. The percentages of aluminium and chromium are balanced to provide high corrosion resistance without compromising the ductile behaviour and fabricability of the material.

The samples have M4 threads on both sides and a notch of 0.05 mm depth and 0.3 mm width in the middle (Figure 3.1.1). The notch increases the local stress, thus the purpose of the notch is to force the deformation and subsequent fracture in the notch area where irradiation has been performed. The notch effect is said to influence the behaviour of the ferritic steel T91 (9% Cr) under loading in liquid lead [35], where clear evidence of LME occurred. In comparison, the smooth samples in the same study showed no LME. Thus, in this thesis, the Fe-10Cr-4Al samples tested have a sharp notch, where it is expected to observe embrittlement effects.

Table 3.1.1: Chemical composition of the sample in weight percentage (wt%).

Alloy	Al	Cr	C	RE	Fe
10-4	4	10	<0.03	Ti, Nb, Zr	Bal.

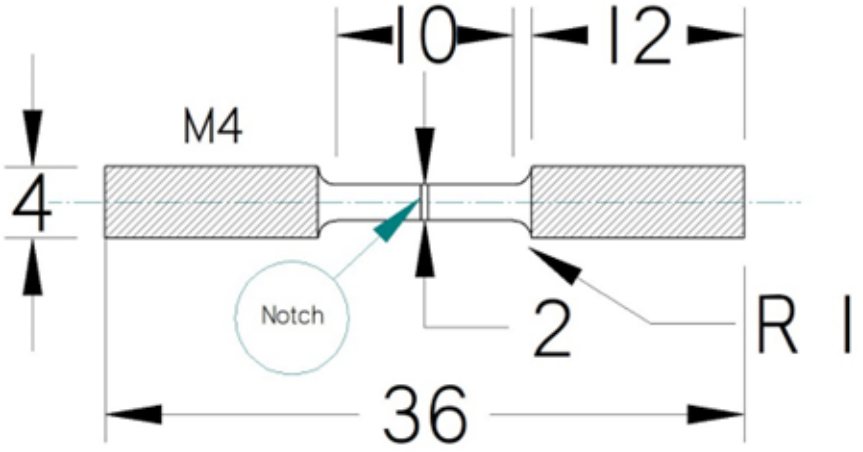

Figure 3.1.1: Fe-10Cr-4Al sample

3.2 Irradiation

3.2.1 Tandem Laboratory at Uppsala University

The samples were irradiated in the Tandem Laboratory at Uppsala University. Protons were delivered by a 5-MV NEC pelletron tandem accelerator that stands out as the most widely applied for standard Ion Beam Analysis (IBA) measurements. The samples are placed in the dedicated chamber where the point of interaction with primary ions can be precisely controlled by moving the sample up along a vertical axis until the beam is focused on the notch. Furthermore, the sample has the freedom of rotation around the vertical axis with a rotation device attached at the bottom to ensure homogeneous exposure on the entire notch surface.

3.2.2 Implantation

For implantation, there were three conditions taken into consideration: maximum possible fluence and energy, homogeneous irradiation, and reasonable irradiation time. For safety purposes, the maximum possible energy was 5.5 MeV and that also provided a reasonably stable current. Due to the high neutron detector readings and the limits that should not be exceeded, the choice of the higher energy of 6 MeV was not possible.

The macrobeam is used for the irradiation to achieve maximal current. The notch lateral area is 1.885 mm^2. However the area irradiated with macrobeam is larger and

it reaches 11 mm^2. The use of the available microbeam was not preferential as the low current would lead to a significant increase in irradiation time. The rest of the irradiation parameters are shown in Table 3.2.1.

Table 3.2.1: Irradiation parameters.

Fluence [ions/cm^2]	3E+17
Area irradiated [mm^2]	11
Dose [nC/mm^2]	4.8E+5
Charge [nC]	5.3E+6
Current [nA]	150 (first sample) 110 (second sample) 92 (third sample) 153 (fourth sample)

For homogeneous irradiation, the rotation device was used that consist of a simple DC motor with a gear. The sample was rotating approximately one revolution per second. In Figure 3.2.1, the wires used for measuring the current are visible. The red spot is the point where the beam went and it was lowered in the chamber to the level of the sample's notch.

The irradiation time varied according to the current, as

$$t[s] = \frac{fluence[ions/cm^2] \cdot charge[C] \cdot area[cm^2]}{current[A]}. \tag{3.1}$$

In order to reach the same dose for all samples, the time was set to 7h for the first sample and 10h for the second and third sample. The beam was very stable during the irradiation of the last sample and the irradiation time was the shortest (approximately 6h).

3.3 Stopping and Range of Ions in Matter (SRIM)

The most commonly used unit for measuring primary radiation damage is the displacements per atom (dpa) parameter. The current internationally recognized standard definition for dpa is derived from the Norgett-Robinson-Torrens (NRT) modification of the Kinchin-Pease model, which was initially proposed to describe defect production [46]. The primary model aimed at calculating the dpa through the

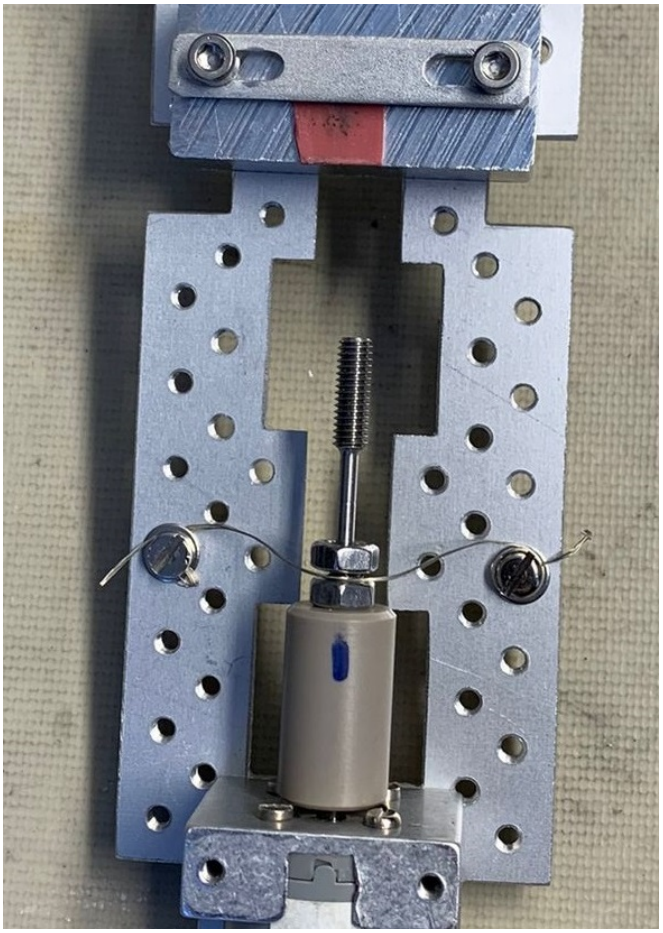

Figure 3.2.1: Sample holder with a rotation device.

analysis of kinetic energy transfers above a material-specific threshold displacement energy. The NRT displacement model became the most successful and widely recognised modification, where the total number of displaced atoms is expressed as

$$N_d = \frac{0.8T_{dam}}{2E_d}, \tag{3.2}$$

with T_{dam} denoting the damage energy and E_d being the threshold displacement energy. While undergoing irradiation, the kinetic energy of the incident ion is transferred to stationary target atoms through atomic collisions. As a consequence of these collisions, the target atom recoils, and is referred to as a primary knock-on atom (PKA). Thus, T_{dam} is the portion of the PKA energy lost by elastic collisions with target atoms. More recent developments and corrections to the NRT dpa have been developed (Nordlund papers on arc-dpa, Yang and Olsson PRM) but for the purpose of this study these modifications are not of great importance to apply here.

For the calculations of dpa and the interactions of energetic ions with a target, the

Monte Carlo simulation-based software The Stopping and Range of Ions in Matter (SRIM) was developed. The Transport of Ions in Matter (TRIM) stands as the most comprehensive program included and it can accommodate complex targets composed of different materials. It calculates the ultimate 3D distribution of ions and a wide range of kinetic phenomena associated with the energy loss of ions including ionization and target damage, all under the assumption of amorphous target materials, thus missing aspects of crystallinity in the damage and ion implantation profiles.

3.3.1 Damage profile

SRIM-2008 code was used to calculate the total number of vacancies for proton irradiation damage with an energy of 5.5 MeV. The energy was chosen based on the safety parameters of the facility, aiming to achieve the maximum energy possible for a stable current. Neutron detection and the precise measurement of ambient dose equivalent play a crucial role in guaranteeing radiation safety in the neutron environments found in neutron-generating facilities, such as particle accelerators. Inside the Tandem Laboratory, the neutron detectors are mounted to monitor the dose to staff and the general public. The higher energy would not be possible due to high neutron readings detected at 6 MeV.

The 'Ion Distribution and Quick Calculation of Damage' is chosen as the type of TRIM calculations. Then, the damage is calculated with the aid of quick statistical estimates according to the Kinchin-Pease (K-P) formalism used in the NRT standard model [47]. Even though the Full Cascade (F-C) option is implied to be more accurate, studies raised some issues such as a mismatch between the damage energy computed using the two options and the number of displacements read out from the code. The difference is more than a factor of two, yet the damage energies derived from the K-P and F-C are comparable. Although both displacement models should predict the same number of displacements for a given damage energy [48]. The calculations were carried out for H ion implantation into the 86wt%Fe-10wt%Cr-4wt%Al layer. The displacement threshold energies for Fe, Cr and Al targets are 40, 40 and 25 eV, respectively [49]. The surface binding energy is set to zero, as the sputtering (removal of surface atoms) is not addressed in this work. The lattice binding energy is the minimum energy required for a recoiling target atom to leave its lattice site. It is set to zero, thus the damage energy is the energy assumed to go into phonons and it is a difference between target atom

energy lost to phonons and the beam energy lost to phonons [48]. SRIM simulations of approximately 10^5 5.5 MeV protons in Fe-10Cr-4Al are shown in Figure 3.3.1.

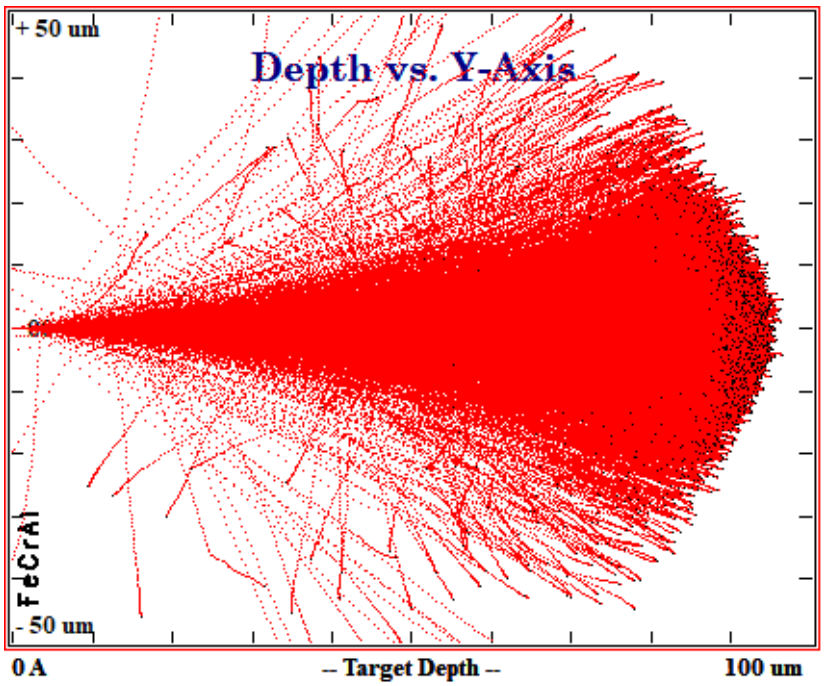

Figure 3.3.1: SRIM calculation of approximately 10^5 ion trajectories for 5.5 MeV proton implanted into Fe-10Cr-4Al

After running TRIM simulations, the damage levels are given in the output file as the sum of the number of vacancies generated by the recoils and by the ions themselves.

3.3.2 Displacements per atom

The energy of the ions is an input parameter and the depth of ion implantation (also referred to as the depth of the peak concentration) into a target can also be found in 'Stopping and Range Tables' in SRIM. Using the same simplified composition of iron, chromium, and aluminum as in Section 3.3.1, the predicted range of protons in the Fe-10Cr-4Al layer is at 88.78 µm.

The radiation-induced damage in units of displacements per atom is shown in Figure 3.3.3. The dpa refers to the number of times that an atom is displaced for a given fluence and can be expressed as:

$$DPA = \frac{fluence[ions/cm^2] \cdot N_v/[Angstrom - ion] \cdot 10^8}{\rho_A[atoms/cm^3]}, \tag{3.3}$$

Ion Energy	dE/dx Elec.	dE/dx Nuclear	Projected Range
5.00 MeV	4.786E-02	2.652E-05	75.80 um
5.50 MeV	4.474E-02	2.441E-05	88.78 um
6.00 MeV	4.206E-02	2.263E-05	102.63 um
6.50 MeV	3.971E-02	2.110E-05	117.33 um

Figure 3.3.2: Predicted implantation depth of H into Fe-10Cr-4Al.

where N_v is the number of generated vacancies and ρ_A is the atomic density which for Fe-10Cr-4Al is 3.685E+22. Fluence is known from the implantation parameters and it is 3E+17 ions/cm^2. The dpa with respect to the depth is shown in Figure 3.3.3. The peak is located at 90 µm where the dpa level is 0.139.

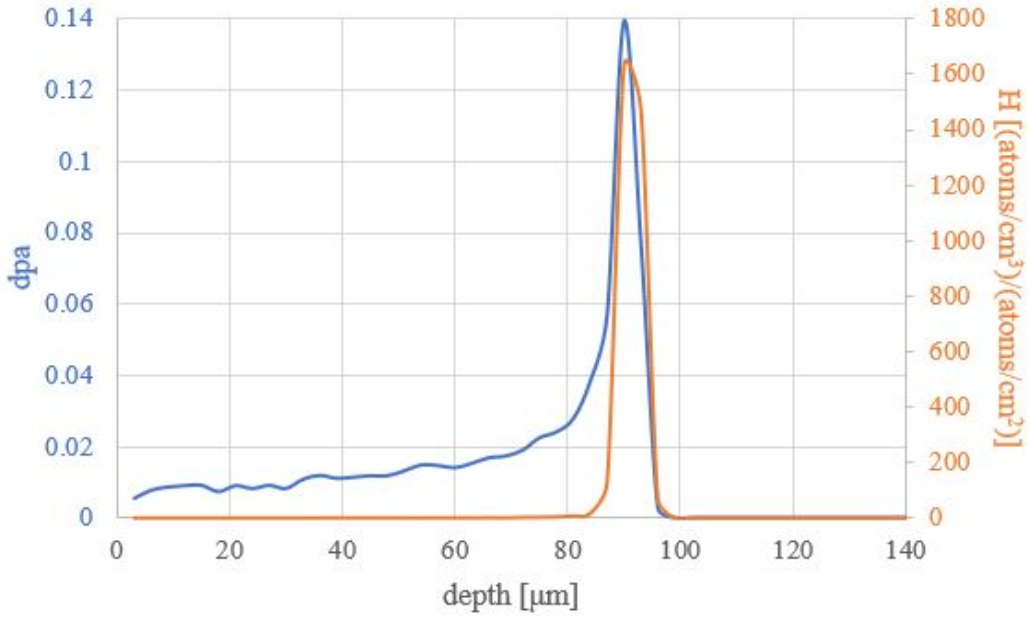

Figure 3.3.3: Displacements per atom for 5.5 MeV proton implantation into Fe-10Cr-4Al.

3.4 Implantation profile with macrobeam

The rotating cylindrical sample leads to a special case of the implantation profile. Implantation with the microbeam would allow for a small implanted area, thus more precise irradiation in the notch. However, it would give a smaller current (1.5 nA), two orders of magnitude lower than with the macrobeam (110-150 nA). The lower current

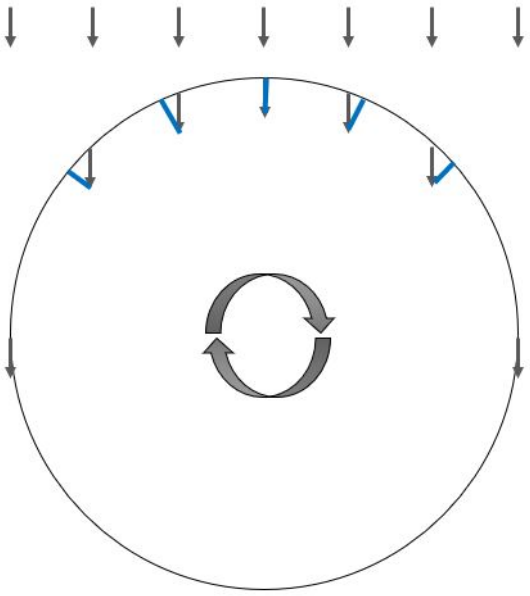

Figure 3.4.1: Schematic of the implantation of a circular rotational sample with macrobeam. Black arrows indicate the trajectory of protons and blue lines are the implantation depth from the surface.

leads to substantial increases in the irradiation time. Thus, the macrobeam with the irradiation area of 11 mm^2 is used, compared to the lateral area of the notch of 1.885 mm^2.

The proton beam trajectory with a penetration depth of around 90 μm does not match the implantation depth from the surface of the cylinder. The latter is in the radial direction, thus depends on the position across the cross-section (Figure 3.4.1). For the continuously rotating sample, the fluence will be sinusoidal between the surface and around 90 μm. The implantation depth profile comes from a function of a circle with the penetration depth taken into consideration,

$$y = \sqrt{r^2 - x^2} - PD, \tag{3.4}$$

where x is the lateral position, r is the radius of the sample and PD is the penetration depth. Then, the relation between the implanted depth and displacements per atom is shown in Figure 3.4.2. It indicates that the real dpa achieved is around 60% of the planned dpa at the peak. The maximum is reached at the Bragg peak as expected but the shape is more parabolic.

Figure 3.4.2 shows the implantation profile for higher energy, 6 MeV that was planned at the beginning. Then, the energy was lowered due to too high neutron reading

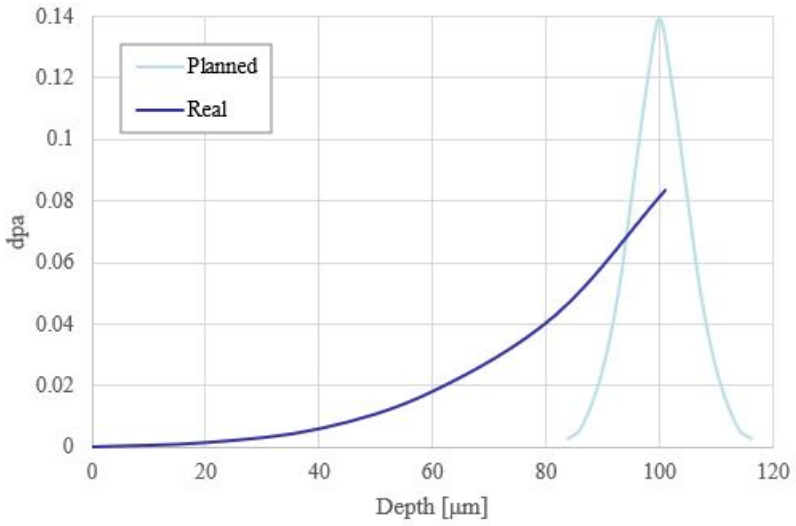

Figure 3.4.2: Implantation profile for real and planned implantation depth with respect to dpa.

detected at the facility at the start of the irradiation, as mentioned in Section 3.3.1.

3.5 Slow Strain Rate Testing (SSRT) rig

The SSRT rig was developed at KTH to test the mechanical properties of various steels. The most important parts of the set-up are the precision linear actuator, load cell, drawbar, gas-tight expansion joint, U-shaped bracket, and the vessel, shown in Figure 3.5.1. The components that are in direct contact with liquid lead, such as the drawbar and U-bracket, are made of Fe-10Cr-4Al to avoid the corrosion of those crucial parts and to extend the lifetime of the rig. The precision linear actuator used to control the strain rate is a model PC40 made by Thomson. It has the maximum possible load of 6000 N and a stroke length of 1200 mm [50]. The electrical actuator provides higher accuracy, easier maintenance, and is more compact than the hydraulic alternatives. The gas-tight expansion joint allows the up-and-down movement of the drawbar without any gas leakage. The drawbar is divided into two parts with the bottom part being submerged in the liquid lead and the holes drilled to place the sample at the end. Made of Fe-10Cr-4Al, the U-shaped bracket holds the sample in place while the load is applied. The sample is screwed by a bolt to the U-bracket and then submerged in the liquid lead. The gas-tight environment is ensured by using copper and Inconel seals. The load cell is connected to the computer and used to measure the forces.

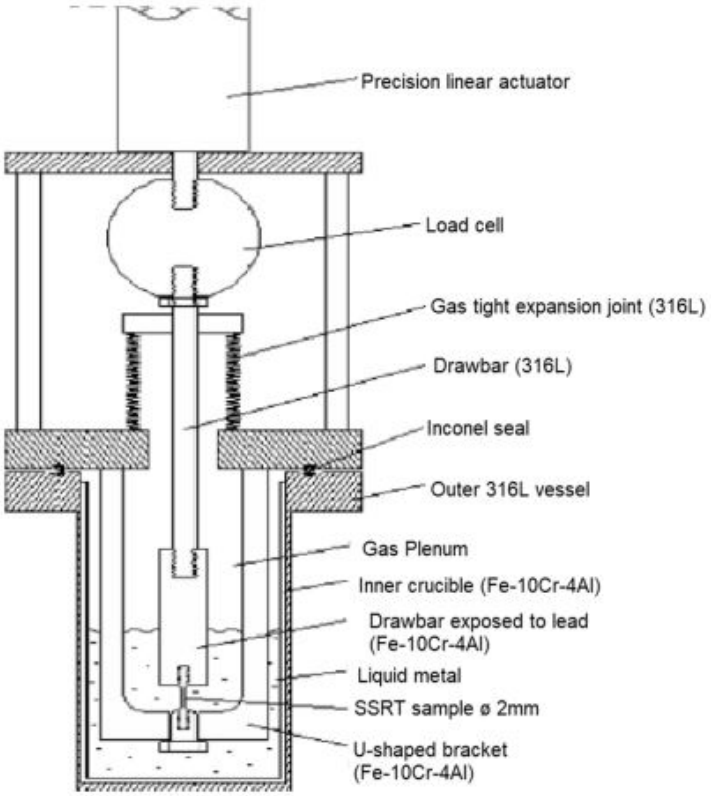

Figure 3.5.1: The SSRT rig set-up.

3.5.1 Experiment parameters

Changing the strain rate from $5 \cdot 10^{-5}$ s^{-1} to $5 \cdot 10^{-4}$ s^{-1} or $5 \cdot 10^{-6}$ s^{-1} has no evident effect on the tensile behaviour and fracture mode, thus the slight changes do not influence the results of the tensile mechanical properties [36]. The 10^{-5} s^{-1} strain rate was deliberately chosen based on prior studies that demonstrated its effectiveness in revealing LME in LBE at temperatures tested earlier [37].

The choice of temperature for this study was based on the ductility trough of the same sample tested in LBE by C. Petersson et al. (2023) [37]. The worst fracture elongation was observed at 375^{o}C. The second test is conducted at 450^{o}C, as the safe choice for temperature where the sample in LBE was shown to recover the normal level of ductility. The irradiated reference samples were tested in the air at 382^{o}C and 455^{o}C.

Before testing in the liquid lead, the samples were wetted in the metal at 450^{o}C for 24h to ensure close contact between the solid sample and the liquid metal. The test until a fracture took 57 min for both samples. Then, the samples were removed and cleaned in the solution of acetic acid ($C_2H_4O_2$), hydrogen peroxide (H_2O_2), and deionized water

in a ratio of 1:1:7. They were left in the solution for 45 min up to 1 h and then rinsed in deionized water.

Chapter 4

Result

4.1 Tensile tests

The SSRT data are plotted in the graph in terms of stress and strain. The engineering stress is the applied load on the original cross-section area of the sample,

$$\sigma = \frac{F}{A_0}, \tag{4.1}$$

where F is the force applied and A_0 is the original cross-sectional area of the sample. The engineering strain refers to the amount that a material deforms in the direction of applied force per unit length and is expressed as

$$\epsilon = \frac{\Delta L}{L_0}, \tag{4.2}$$

where L_0 is the original value of the gauge length and ΔL represents a change in length. The engineering stress-strain curve shows three points of interest, marked in Figure 4.1.1. Point A is the yield strength (YS) that refers to the stress at which a material ceases its elastic deformation and transitions into plastic deformation. After passing the yield point, the sample becomes permanently deformed and eventually reaches Point B, which is the ultimate tensile strength (UTS). Then, UTS is the maximum stress that the sample can withstand while being stretched before breaking. For ductile materials, this is where necking starts as the type of plastic deformation characterized by a localized reduction in the cross-sectional area. The necking zone continues until Point C, which denotes the sample fracture.

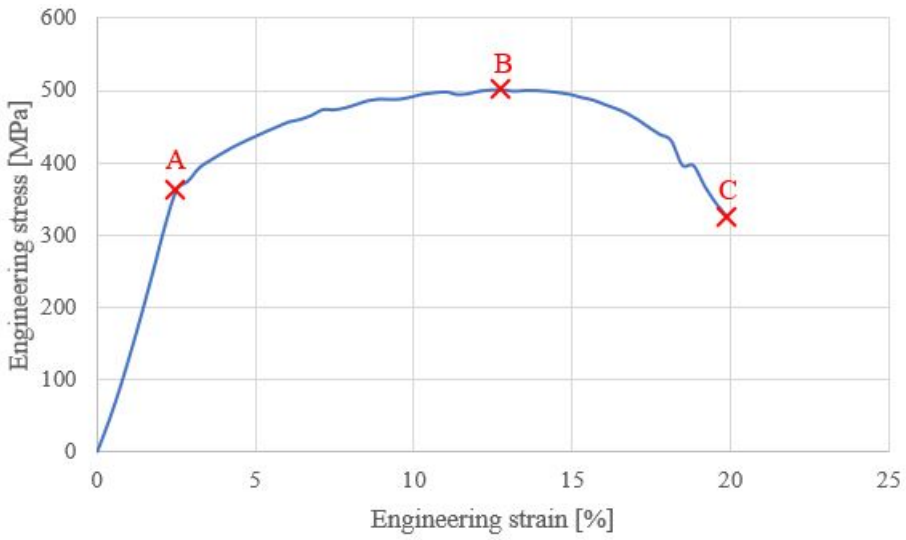

Figure 4.1.1: Engineering stress-strain curve for Fe-10Cr-4Al sample tested at 375°C.

The results of the SSRT are presented on the engineering stress-strain curves and the characteristics of irradiated Fe-10Cr-4Al, such as yield strength, ultimate tensile strength and total elongation to failure, are shown in Table 4.1.1. Figure 4.1.2 shows both irradiated samples tested in the liquid lead at 375°C and 450°C.

Table 4.1.1: SSRT data for yield strength, ultimate tensile strength, and fracture elongation for the samples tested in liquid lead and the air.

T[°C]	Condition	YS [MPa]	UTS [MPa]	Total elongation to failure [%]	Ref.
375	Pb	358	472	24.99	[37]
375	Irradiation + Pb	362	500	19.88	
382	Irradiation + Air	361	502	19.83	
450	Pb	361	476	25.11	[37]
450	Irradiation + Pb	348	461	21.77	
455	Irradiation + Air	354	470	21	

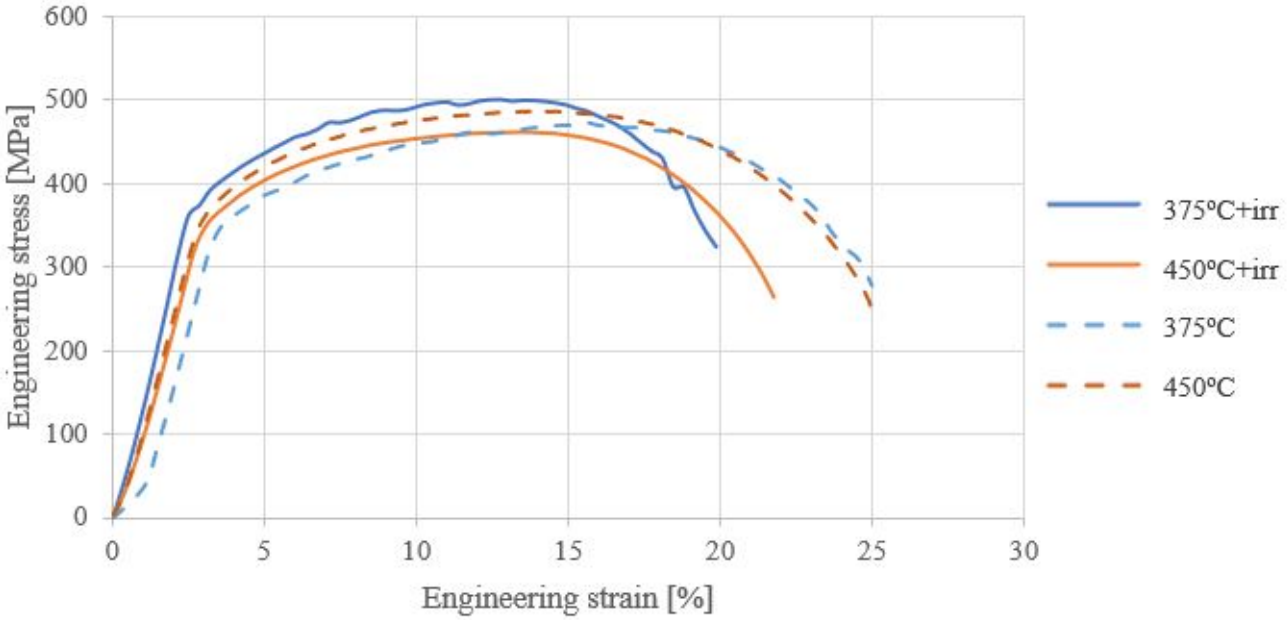

Figure 4.1.2: Engineering stress-strain curve for samples tested in the liquid lead at two different temperatures.

The data can be compared with Fe-10Cr-4Al tested in liquid lead without prior irradiation found in the literature [37](Table 4.1.1). For 375^{o}C, the yield strength and ultimate tensile strength increase for the irradiated sample, as expected. This indicates that radiation hardens the sample slightly, leading to an increase in its strength, which consequently results in a reduction of the fracture toughness. The total elongation to failure decreases 5.11% compared to the unirradiated sample.

The general trend of decreasing UTS and YS with temperature is expected as it indicates the higher internal energy of atoms that vibrate more vigorously. The thermal activation of dislocation motion leads to easier plastic deformation due to less stress required to move the dislocation from their equilibrium positions. It explains a reduction of YS and UTS for the tests at 450^{o}C. The same sample experienced a loss of tensile elongation by 3.34% compared to the reported unirradiated sample [37]. Compared to the unirradiated samples, there is a larger effect of temperature on YS and UTS. The irradiated samples tested at 450^{o}C show a decrease of approximately 4% in YS and 8% in UTS, while unirradiated samples vary by 1%, compared to the Fe-10Cr-4Al tested at 375^{o}C. This could be an effect of irradiation softening of the alloy at higher temperatures, as mentioned in Section 2.2.2.

The reference samples tested in air at similar temperatures, 385^{o}C and 455^{o}C, are shown in Figure 4.1.3. The effect of increasing temperature is again more prominent

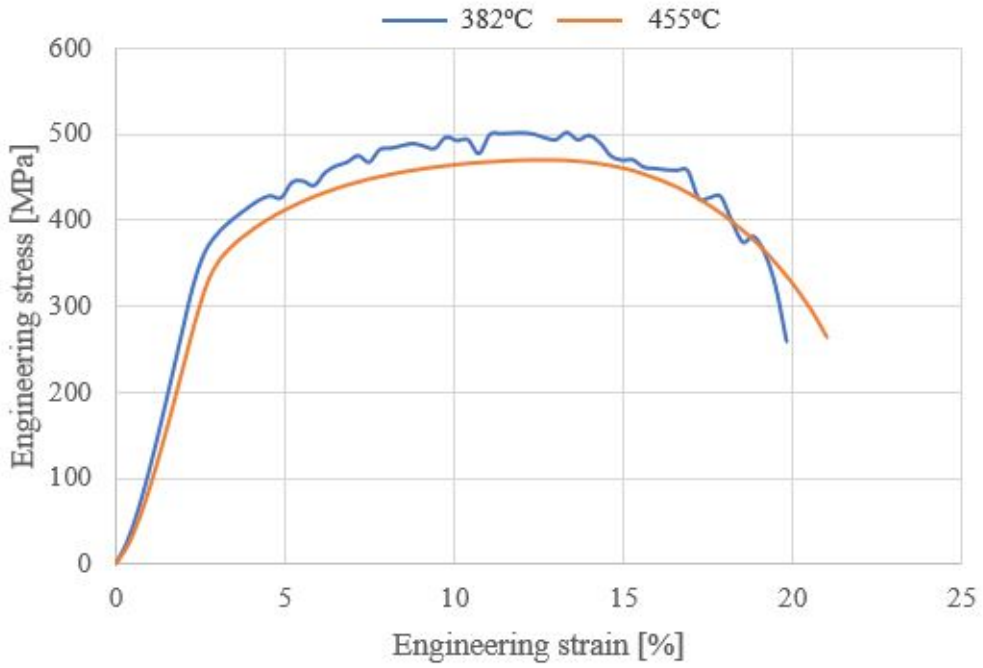

Figure 4.1.3: Engineering stress-strain curve for irradiated samples tested in air.

for YS and UTS, compared to the unirradiated samples tested in lead. The SSRT results demonstrate nearly identical mechanical properties for irradiated samples tested at a lower temperature in air and in lead. This might be an indication of absence of LME, as the sample in lead is not additionally affected. The specimen tested at 455^{o}C fractured far away from the notch, approximately 3mm away. The radiation spot size was around 1.5 mm, thus the breakage is far outside of the irradiation area. This could the be reason for the slightly lower total elongation to failure compared to a sample tested in lead. However, as the sample did not break in the notch, an exact comparison is not possible. The un-notched fracture is most probably the result of the manufacturing process of the sample and the issue arose due to the pre-existing defects. According to our experience, it is not that unusual to happen and the same Fe-10Cr-4Al samples fractured outside of the notch in the past.

4.2 Fracture surface analysis

The fracture surface features were studied using Scanning Electron Microscopy (SEM). The images of the samples tested in air at 382^{o}C are shown in Figure 4.2.1. The overview shows a fracture in the process of cup-cone breakage, which is a type of failure commonly observed in ductile metals when they are subjected to a uniaxial force

[51]. The fracture surface exhibits a distinctive dimpled surface morphology, which is a characteristic feature of a ductile fracture (Figure 4.2.1B) and includes microvoid nucleation, growth, and coalescence. As the penetration depth of protons is around 90μm, thus it is important to have a closer look at the edges of the notched fracture. In some regions at the edge, the failure is ductile with dimple formations (Figure 4.2.1C), whereas in other spots the fracture seems more brittle (Figure 4.2.1D). In the latter, grains appear larger, and more placed in sections. The cleavage steps were also observed and marked. There is a mix of intergranular (a crack propagates along the grain boundaries) and transgranular (the crack grows through the material grains) cracking.

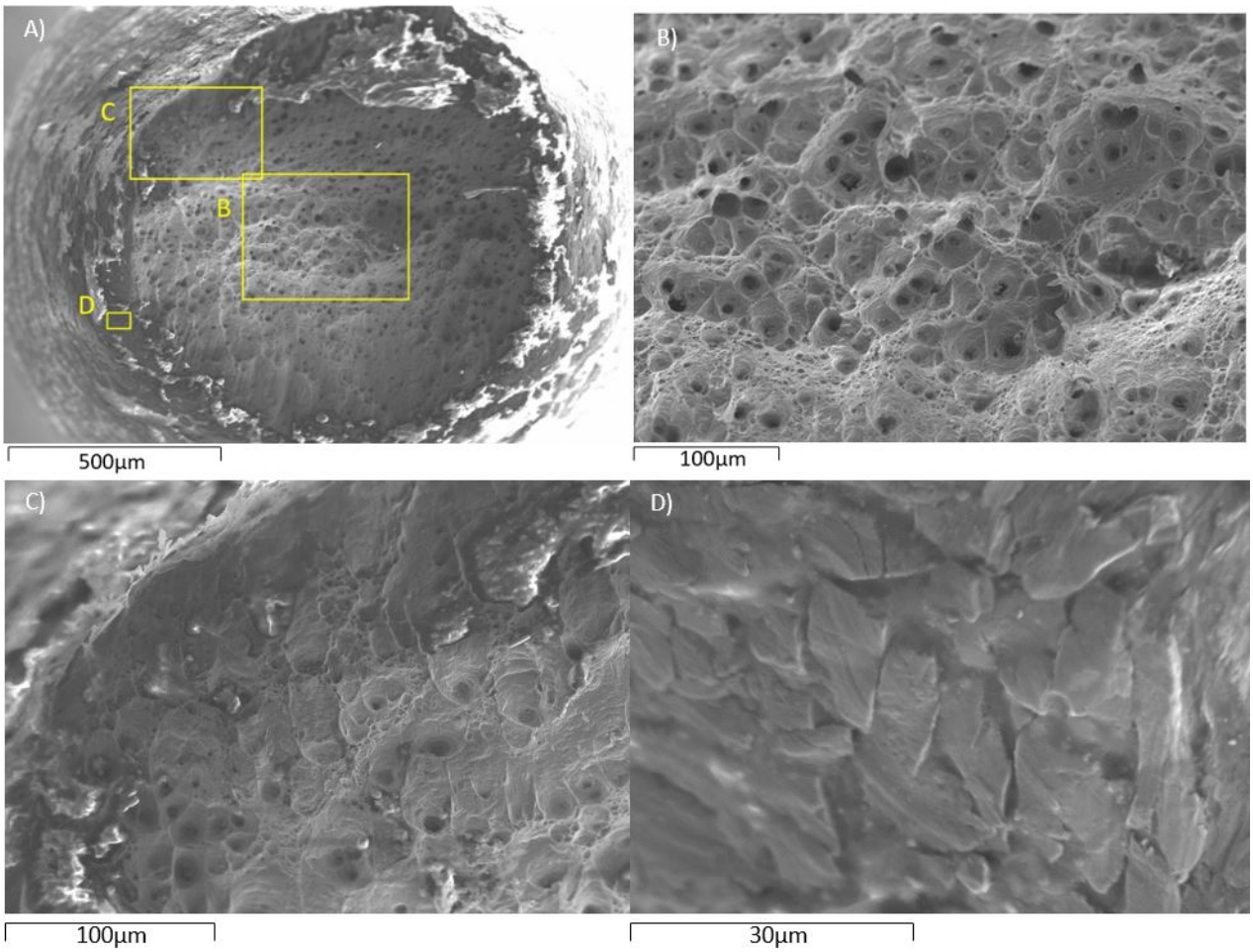

Figure 4.2.1: The SEM images of the fracture surfaces of the sample tested in air at 382^{o}C A) the overview, B) surface view in the centre, C-D) on the edges.

All the samples show a ductile dimpled behaviour in the centre. The LME appears as a brittle fracture mode in the centre, which is not the case for the tested samples. This could indicate absence of LME, however, other scenarios such as hydrogen or radiation embrittlement are still possible. Moreover, the SEM images indicate similar brittle

structures at the edges for all irradiated samples. In Figure 4.2.2B, the clear transition from ductile to brittle is visible. The ductile behaviour with dimples on the left and more granular structures for a brittle break towards the right side of the image. It is common to see a mix of ductile and brittle fracture structures. There are many factors, such as strain rate, local composition and grain orientation, affecting the breakage and making it not fully ductile nor brittle.

The edge is unclear, thus the brittle behaviour appears a little further away from the implantation depth of protons. However, Figure 4.2.2C clearly indicates the flat brittle structures close to the edge, also found in Figure 4.2.1D. Those facets, which are flat surfaces on the fracture surface, are seen on the edges of all samples that broke in the notch.

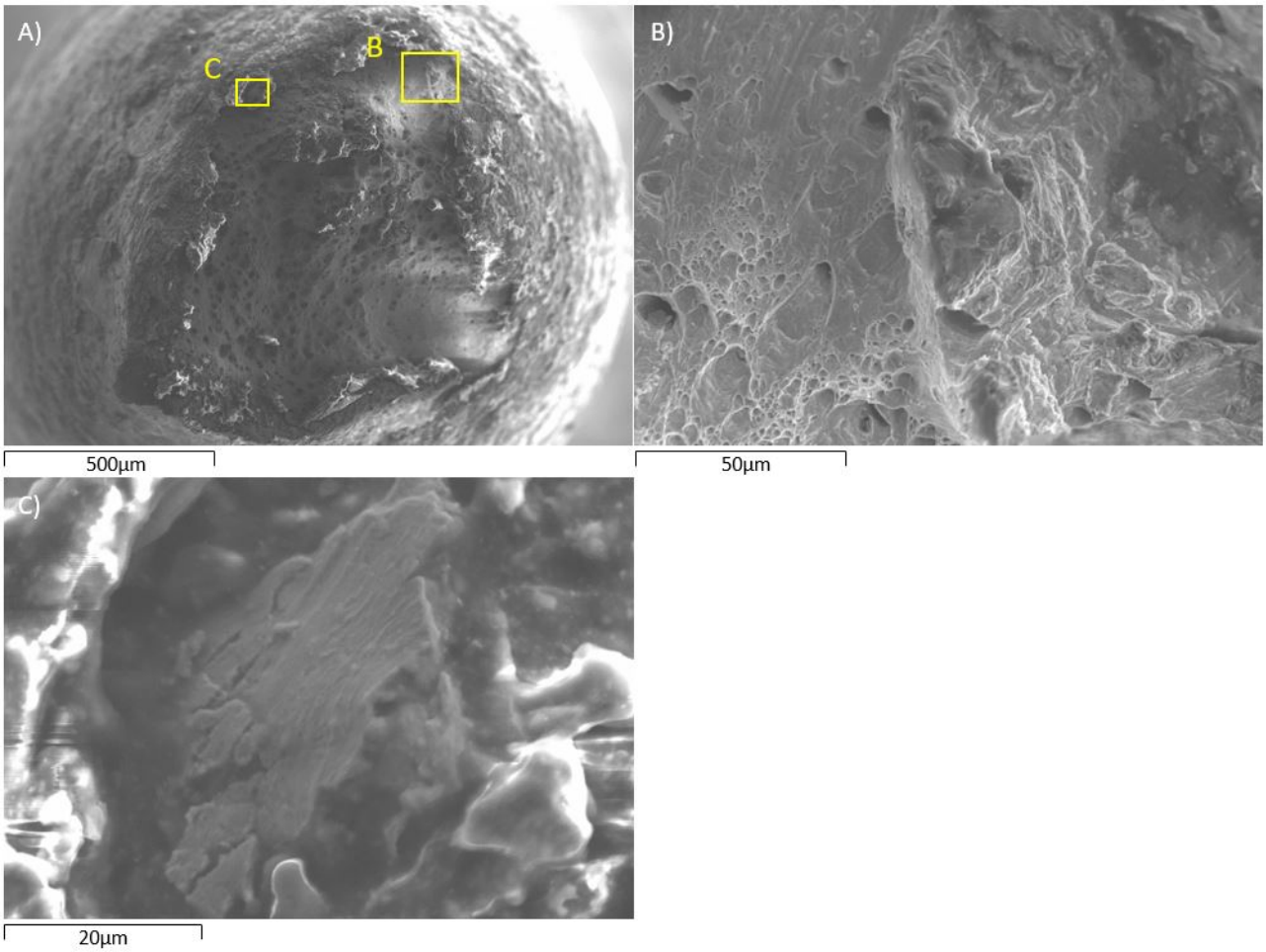

Figure 4.2.2: The SEM images of the fracture surface of the sample tested in lead at 375^{o}C A) the overview, B-C) on the edges.

The sample at 450^{o}C gives similar results with ductile fracture mode at the centre. Figure 4.2.3B shows the close-up to the middle section. There are some Pb leftovers,

which is quite usual as the sample was tested in Pb and the cleaning solution did not remove all Pb from the surface. The oxides and carbides are present as well in other spots. The dimpled structure is seen where the grains were pulled away, Figure 4.2.3C. Figure 4.2.3D shows again similar brittle formation as previously seen in Pb 375^{o}C and air 382^{o}C.

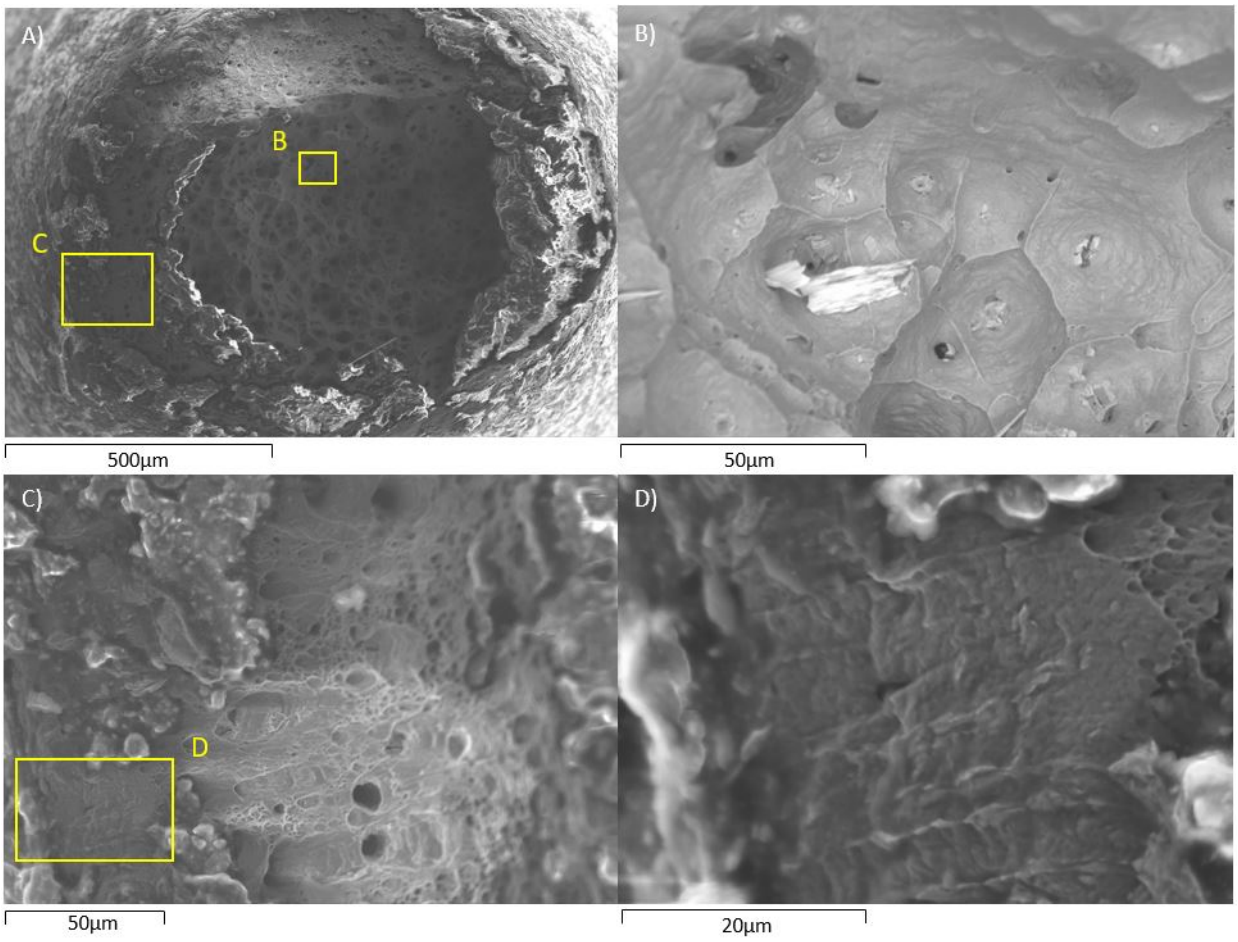

Figure 4.2.3: The SEM images of the fracture surface of the sample tested in lead at 450^{o}C A) the overview, B) surface view in the centre, C) the edge area, D) magnified view of the brittle structure.

Chapter 5

Discussion

5.1 Irradiation effect on fracture elongation

The choice of temperatures for tensile testing of the irradiated sample was based on the features of the ductility trough of Fe-10Cr-4Al in LBE environment [37]. The samples in liquid lead show no reduction in elongation [37]. However, the irradiated samples exhibit a significant decrease in the total elongation to failure compared to unirradiated samples (Figure 5.1.1). Moreover, there is a slight increase in fracture elongation (1.89%) with respect to the increasing temperature.

The reduced elongation can result from different phenomena, such as radiation damage, hydrogen, and liquid metal embrittlement, mentioned in Section 2.3. The occurrence of LME is very unlikely as the SEM images do not show the brittle crack initiation structures that would be expected in that scenario. Moreover, there seems to be very little effect of the environment during the tensile test on the loss of elongation. The irradiation and proton implantation is the common factor. The reference fracture surface with a brittle crack propagation that proved LME in LBE can be seen in Figure 5.1.2. The structure is different compared to the edge surface brittle regions in irradiated samples (Figure 4.2.1D and Figure 4.2.2C). Moreover, in LME the brittle structures are shown in the centre of the sample, whereas all irradiated samples in this work exhibit ductile behaviour inside.

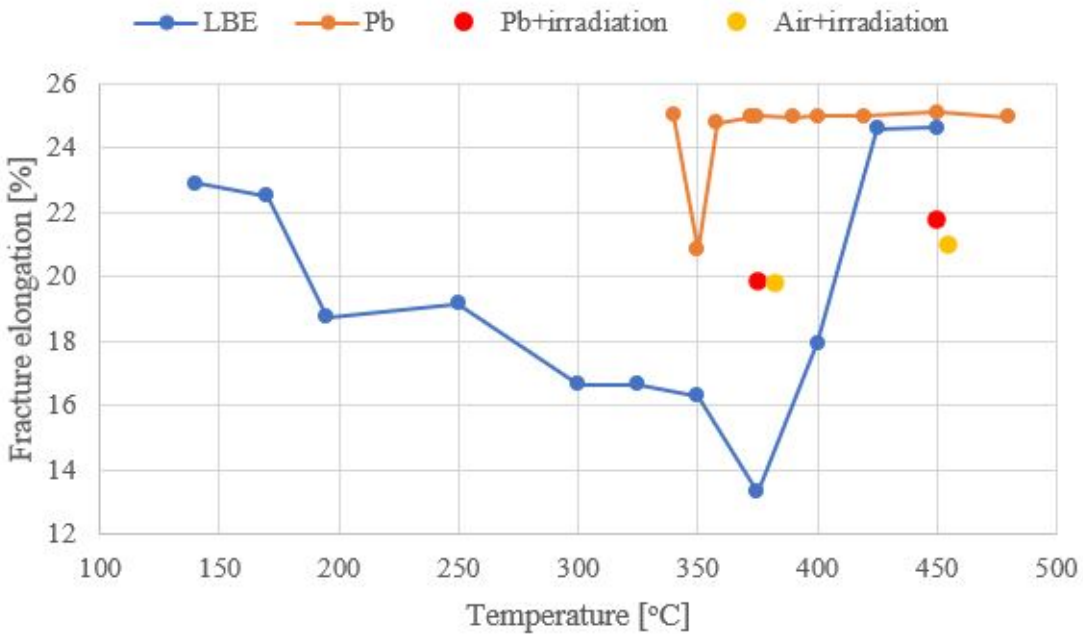

Figure 5.1.1: The fracture elongation as a function of temperature for irradiated samples and the reference from the literature for unirradiated samples tested in LBE and Pb [37].

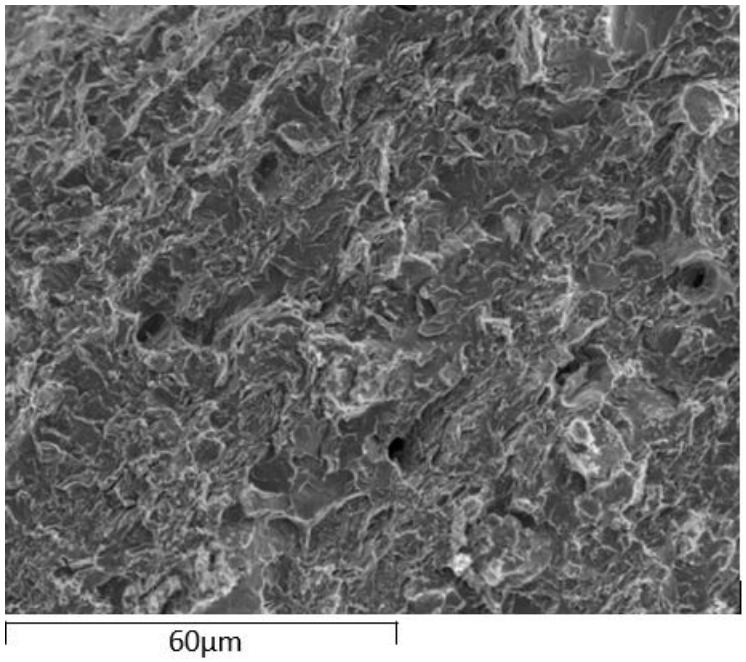

Figure 5.1.2: Brittle fracture surface of Fe-10Cr-4Al tested in LBE at 400°C. Extracted from [37].

Chromium in the alloy composition promotes the diffusion of aluminium towards the surface, as the faster formation of chromia makes the surface slightly Cr-depleted. Chromium facilitates the formation of alumina oxide by providing protection and allowing sufficient time for its development. The diffusion of chromium from the bulk is considerably slower than that of aluminium, which causes the latter to diffuse towards the surface and thus restore the relative Al concentration beneath the oxide layer [52]. Thus, Cr oxide forms first, followed by the subsequent formation of Al oxide underneath.

It can be assumed that there might still be the presence of an oxide layer after the wetting process. The fast diffusion of aluminium to the surface makes it possible to restore the oxide layer preventing close contact between the sample and liquid lead, thus restraining the LME. The regions with substantial amount of oxides can be seen in Figure 4.2.1A, where white areas on the edge (clearly visible on the right side of the sample) indicate the oxygen presence.

The embrittlement phenomena still considered for the irradiated Fe-10Cr-4Al tested in the lead environment at elevated temperatures are radiation and hydrogen embrittlement. The latter might be caused by the large amount of hydrogen implanted during the irradiation. In the nuclear reactor, this would not be an issue as the main source of the irradiation are neutrons. Protons were only used in the experiment as they are less expensive, compared to neutron irradiation. However, the SEM images indicate the existence of features common for a brittle fracture mode on the edges (in the irradiation area). As mentioned in Section 2.3.2, flat surfaces like intergranular facets and voids are frequent characteristics of hydrogen embrittlement.

5.2 Future Work

Further investigation of the brittle regions with a higher-resolution SEM would be beneficial. In Figure 4.2.1D, the structure shows an example of a path in the middle of the SEM image that could be examined closer. Moreover, due to the un-notched fracture of the sample tested at 455°C in air, there is a possibility of examining the unaffected irradiation area. Nano-indentation to measure radiation induced hardness would be one such examination. The sample could also be cut in the notch and then polished. Considering the beam spot size being larger than a notch, thus careful polishing is possible without losing the irradiated region. Later, the sample can be

examined with electron backscatter diffraction (EBSD) to investigate grain boundaries and local orientation.

To improve the understanding of irradiated FeCrAl in reactor conditions, neutron irradiation tests would be beneficial. Neutrons would go through the sample, in comparison to protons that induce surface phenomena and stop inside the sample as they have limited penetration depth. However, the sample used in this study is too thick to mimic the neutron behaviour. Thus, it would be beneficial to develop thin enough samples to investigate the effect of neutron irradiation. Micro-sizing the sample and using a microbeam for the irradiation of a very small area, would give a more homogeneous implantation and could avoid the hydrogen implantation, if the sample is thin enough.

Chapter 6

Conclusions

The Fe-10Cr-4Al samples irradiated with protons up to 0.14 dpa show a reduction in ductility after testing in liquid lead and air at elevated temperatures. The total elongation to failure for irradiated Fe-10Cr-4Al decreases by 5.11% and 3.34% for liquid lead temperatures of 375^{o}C and 450^{o}C, respectively. The air tests show quite similar behaviour for samples tested at similar temperatures, 382^{o}C and 455^{o}C. Moreover, the results indicate that the changes in temperature have a larger effect on the irradiated samples, compared to the literature unirradiated data. The tests in lead showed an increase in fracture elongation by 1.89%, in comparison to 0.12% for the reference unirradiated samples. The reason could be a slight ductility recovery at the higher temperature for the more affected irradiated samples.

The samples were irradiated at the notch with a hydrogen penetration depth of 90μm, which is also an area of interest while examining samples with SEM. The embrittlement phenomena considered were LME, radiation induced embrittlement and hydrogen embrittlement. The theory of LME was rejected as all Fe-10Cr-4Al samples show ductile breaking mode in the centre, which is unusual for this type of embrittlement. The common feature of the results indicate that the radiation is the driving force for the loss of elongation. The SEM images showed brittle fracture mode at the edges of the samples that broke in the irradiated zone around the notch. Features such as flat facets or voids are common for hydrogen embrittlement, thus it is possible that there are signs of implanted hydrogen effect on the edges of the samples. Further investigation with higher-resolution SEM would be beneficial to confirm the conclusion.

Bibliography

[1] IPCC. *Special Report on Global Warming of 1.5 °C*. 2017. URL: https://www.ipcc.ch/sr15/.

[2] *Our World in Data. Electricity Mix*. Accessed: 2023-03-15. URL: https://ourworldindata.org/electricity-mix.

[3] *World Nuclear Association. World Nuclear Performance Report 2022*. No. 2022/003. 2022.

[4] *Bisconti Research. Record High Public Support for Nuclear Energy, 2022 National Nuclear Energy Public Opinion Survey Finds*. Accessed: 2023-03-21. 2022. URL: https://www.bisconti.com/blog/public-opinion-survey-finds.

[5] Analysgruppen. *What is your personal opinion about the future use of nuclear power as energy source in Sweden?* Accessed: 2023-03-27. 2022. URL: https://www.analys.se/engelska/opinion-polls/.

[6] WHO. *Chernobyl: the true scale of the accident*. Accessed: 2023-03-27. 2005. URL: https://apps.who.int/mediacentre/news/releases/2005/pr38/en/index1.html.

[7] *Our World in Data. Death rates per unit of electricity production*. Accessed: 2023-03-27. URL: https://ourworldindata.org/grapher/death-rates-from-energy-production-per-twh.

[8] *Generation IV International Forum. Gen IV Reactor Design*. Accessed: 2023-03-28. URL: https://www.gen-4.org/gif/jcms/c_40275/gen-iv-reactor-design.

[9] *Generation IV International Forum. Generation IV Goals*. Accessed: 2023-03-28. URL: https://www.gen-4.org/gif/jcms/c_9502/generation-iv-goals.

[10] *World Nuclear Association. Generation IV Nuclear Reactors*. Accessed: 2023-03-28. URL: https://world-nuclear.org/information-library/nuclear-fuel-cycle/nuclear-power-reactors/generation-iv-nuclear-reactors.aspx.

[11] *Generation IV International Forum. Lead-Cooled Fast Reactor (LFR)*. Accessed: 2023-03-31. URL: https://www.gen-4.org/gif/jcms/c_42149/lead-cooled-fast-reactor-lfr.

[12] Alemberti A., et al. *GIF-LFR System Safety Assessment*. 2020.

[13] Ejenstam, Jesper and Szakálos, Peter. "Long term corrosion resistance of alumina forming austenitic stainless steels in liquid lead". In: *Journal of Nuclear Materials* 461 (2015), pp. 164–170. ISSN: 0022-3115. DOI: 10.1016/j.jnucmat.2015.03.011. URL: https://www.sciencedirect.com/science/article/pii/S0022311515001555.

[14] Guo, Xianglong, Chen, Kai, Gao, Wenhua, Shen, Zhao, and Zhang, Lefu. "Corrosion behavior of alumina-forming and oxide dispersion strengthened austenitic 316 stainless steel in supercritical water". In: *Corrosion Science* 138 (2018), pp. 297–306. ISSN: 0010-938X. DOI: https://doi.org/10.1016/j.corsci.2018.04.026.

[15] Field, Kevin G., Snead, Mary A., Yamamoto, Yukinori, and Terrani, Kurt A. *Handbook on the Material Properties of FeCrAl Alloys for Nuclear Power Production Applications (FY18 Version: Revision 1)*. 2018. DOI: 10.2172/1474581. URL: https://www.osti.gov/biblio/1474581.

[16] Dömstedt, Peter, Lundberg, Mats, and Szakálos, Peter. "Corrosion studies of a low alloyed Fe–10Cr–4Al steel exposed in liquid Pb at very high temperatures". In: *Journal of Nuclear Materials* 531 (2020), p. 152022. ISSN: 0022-3115. DOI: 10.1016/j.jnucmat.2020.152022. URL: https://www.sciencedirect.com/science/article/pii/S0022311519314023.

[17] Ejenstam, Jesper, Halvarsson, Mats, Weidow, Jonathan, Jönsson, Bo, and Szakalos, Peter. "Oxidation studies of Fe10CrAl–RE alloys exposed to Pb at 550°C for 10,000h". In: *Journal of Nuclear Materials* 443.1 (2013), pp. 161–170. ISSN: 0022-3115. DOI: 10.1016/j.jnucmat.2013.07.023. URL: https://www.sciencedirect.com/science/article/pii/S0022311513009112.

[18] Kelton, K.F. and Greer, A.L. “Chapter 14 - Transformations in the Solid Phase”. In: *Nucleation in Condensed Matter*. Ed. by K.F. Kelton and A.L. Greer. Vol. 15. Pergamon Materials Series. Pergamon, 2010, pp. 511–586. DOI: 10.1016/S1470-1804(09)01514-4. URL: https://www.sciencedirect.com/science/article/pii/S1470180409015144.

[19] Was, G.S. *Simulation of Neutron Irradiation Effects with Ions. Fundamentals of Radiation Materials Science: Metals and Alloys*. Berlin, Heidelberg: Springer Berlin Heidelberg, 2007, pp. 545–577. ISBN: 978-3-540-49472-0. DOI: 10.1007/978-3-540-49472-0_11.

[20] Was, G.S, Busby, J.T, Allen, T, Kenik, E.A, Jensson, A, Bruemmer, S.M, Gan, J, Edwards, A.D, Scott, P.M, and Andreson, P.L. “Emulation of neutron irradiation effects with protons: validation of principle”. In: *Journal of Nuclear Materials* 300.2 (2002), pp. 198–216. ISSN: 0022-3115. DOI: 10.1016/S0022-3115(01)00751-6. URL: https://www.sciencedirect.com/science/article/pii/S0022311501007516.

[21] Was, G.S. “Challenges to the use of ion irradiation for emulating reactor irradiation”. In: *Journal of Materials Research* 30 (2015), pp. 1158–1182. URL: https://doi.org/10.1557/jmr.2015.73.

[22] Wang, Peng, Bowman, Josh, Bachhav, Mukesh, Kammenzind, Bruce, Smith, Richard, Carter, Jesse, Motta, Arthur, Lacroix, Evrard, and Was, Gary. “Emulation of neutron damage with proton irradiation and its effects on microstructure and microchemistry of Zircaloy-4”. In: *Journal of Nuclear Materials* 557 (2021), p. 153281. ISSN: 0022-3115. DOI: 10.1016/j.jnucmat.2021.153281. URL: https://www.sciencedirect.com/science/article/pii/S0022311521005043.

[23] *Total Materia. Irradiation Effects on Ferritic Martensitic Steels: Part Two*. Accessed: 2023-05-22. URL: https://www.totalmateria.com/page.aspx?ID=CheckArticle&site=kts&NM=249.

[24] Luzginova, N.V., Rensman, J.-W., Jong, M., ten Pierick, P., Bakker, T., and Nolles, H. “Overview of 10 years of irradiation projects on Eurofer97 steel at High Flux Reactor in Petten”. In: *Journal of Nuclear Materials* 455.1 (2014). Proceedings of the 16th International Conference on Fusion Reactor Materials (ICFRM-16), pp. 21–25. ISSN: 0022-3115. DOI: 10.1016/j.jnucmat.2014.

03.028. URL: https://www.sciencedirect.com/science/article/pii/S0022311514001378.

[25] Xiao, Xiazi. "Fundamental Mechanisms for Irradiation-Hardening and Embrittlement: A Review". In: *Metals* 9.10 (2019). ISSN: 2075-4701. DOI: 10.3390/met9101132. URL: https://www.mdpi.com/2075-4701/9/10/1132.

[26] Martin, May L., Connolly, Matthew J., DelRio, Frank W., and Slifka, Andrew J. "Hydrogen embrittlement in ferritic steels". In: *Applied Physics Reviews* 7.4 (Oct. 2020). 041301. ISSN: 1931-9401. DOI: 10.1063/5.0012851. URL: https://doi.org/10.1063/5.0012851.

[27] J, Volkl and G, Alefeld. In: *Diffusion in solids: recent developments*. Ed. by A. S. Norwick and Burton J.J. Academic Press, New York, 1975, p. 231.

[28] Neeraj, T., Srinivasan, R., and Li, Ju. "Hydrogen embrittlement of ferritic steels: Observations on deformation microstructure, nanoscale dimples and failure by nanovoiding". In: *Acta Materialia* 60.13 (2012), pp. 5160–5171. ISSN: 1359-6454. DOI: https://doi.org/10.1016/j.actamat.2012.06.014. URL: https://www.sciencedirect.com/science/article/pii/S135964541200376X.

[29] Song, Jun and Curtin, W A. "Atomic mechanism and prediction of hydrogen embrittlement in iron". In: *Nature materials* 12.2 (2013), pp. 145–151. ISSN: 1476-1122.

[30] Xu, Kang and Rana, Mahendra. "Tensile and fracture properties of carbon and low alloy steels in high pressure hydrogen". In: *Proceedings of the 2008 International Hydrogen Conference - Effects of Hydrogen on Materials* (2009), pp. 349–356. URL: https://www.scopus.com/inward/record.uri?eid=2-s2.0-77649125784&partnerID=40&md5=de00a60dc16608ed6ef0886c2dce1b53.

[31] Robertson, Ian M., Sofronis, P., Nagao, A., Martin, M. L., Wang, S., Gross, D. W., and Nygren, K. E. "Hydrogen Embrittlement Understood". In: *Metallurgical and Materials Transactions A* 46 (2015). DOI: 10.1007/s11661-015-2836-1.

[32] Commission, European, Centre, Joint Research, Hojna, A, and Nilsson, K. *Overview of mechanisms models for liquid metal embrittlement and future directions*. Publications Office, 2018. DOI: 10.2760/017392.

[33] Wang, Frederick E. “Chapter 6 - Mechanical Properties”. In: *Bonding Theory for Metals and Alloys (Second Edition)*. Ed. by Frederick E. Wang. Second Edition. Elsevier, 2019, pp. 157–191. ISBN: 978-0-444-64201-1. DOI: 10.1016/B978-0-444-64201-1.00006-3.

[34] Fazio, C. *Handbook on Lead-bismuth Eutectic Alloy and Lead Properties, Materials Compatibility, Thermal-hydraulics and Technologies: 2015 Edition*. Ed. by Nuclear Enery Agency (NEA). Vol. NEA. No. 7268. Paris (France): OECD, 2016, pp. 494–508.

[35] Hojná, Anna, Di Gabriele, Fosca, Klecka, Jakub, and Burda, Jaroslav. “Behaviour of the steel T91 under uniaxial and multiaxial slow loading in contact with liquid lead”. In: *Journal of Nuclear Materials* 466 (2015), pp. 292–301. ISSN: 0022-3115. DOI: 10.1016/j.jnucmat.2015.05.041. URL: https://www.sciencedirect.com/science/article/pii/S0022311515300209.

[36] Gong, Xing, Chen, Jiajun, Hu, Feiyu, Xiang, Congying, Yu, Zhiyang, Xiao, Jun, Wang, Hui, Gong, Haoran, Wang, Hao, Liu, Chaohong, Deng, Yangbin, Pang, Bo, Huang, Xi, Li, Yongchun, and Yin, Yuan. “Liquid metal embrittlement of an Fe10Cr4Al ferritic alloy exposed to oxygen-depleted and -saturated lead-bismuth eutectic at 350°C”. In: *Corrosion Science* 165 (2020), p. 108364. ISSN: 0010-938X. DOI: 10.1016/j.corsci.2019.108364. URL: https://www.sciencedirect.com/science/article/pii/S0010938X19316154.

[37] Petersson, Christopher, Szakalos, Peter, and Dietrich Stein, Daniel. “Slow strain rate testing of Fe-10Cr-4Al ferritic steel in liquid lead and lead–bismuth eutectic”. In: *Nuclear Materials and Energy* 34 (2023), p. 101403. ISSN: 2352-1791. DOI: 10.1016/j.nme.2023.101403.

[38] Gong, Xing, Hu, Feiyu, Chen, Jiajun, Wang, Hui, Gong, Haoran, Xiao, Jun, Wang, Hao, Deng, Yangbin, Pang, Bo, Huang, Xi, Li, Yongchun, and Yin, Yuan. “Effect of temperature on liquid metal embrittlement susceptibility of an Fe10Cr4Al ferritic alloy in contact with stagnant lead-bismuth eutectic”. In: *Journal of Nuclear Materials* 537 (2020), p. 152196. ISSN: 0022-3115. DOI: 10.1016/j.jnucmat.2020.152196. URL: https://www.sciencedirect.com/science/article/pii/S0022311520302294.

[39] Stein, D. *SSRT of 10-4 FeCrAl in LBE and Pb to Characterize Liquid Metal Embrittlement Effects (Dissertation)*. Accessed: 2023-05-01. 2022. URL: http://urn.kb.se/resolve?urn=urn:nbn:se:kth:diva-315279.

[40] Kamdar, M.H. "Liquid Metal Embrittlement". In: *Embrittlement of Engineering Alloys*. Ed. by C.L. Briant and S.K. Banerji. Vol. 25. Treatise on Materials Science Technology. Elsevier, 1983, pp. 361–459. DOI: 10.1016/B978-0-12-341825-8.50015-5. URL: https://www.sciencedirect.com/science/article/pii/B9780123418258500155.

[41] Proriol Serre, Ingrid and Vogt, Jean-Bernard. "Liquid metal embrittlement sensitivity of the T91 steel in lead, in bismuth and in lead-bismuth eutectic". In: *Journal of Nuclear Materials* 531 (2020), p. 152021. ISSN: 0022-3115. DOI: 10.1016/j.jnucmat.2020.152021. URL: https://www.sciencedirect.com/science/article/pii/S0022311519315284.

[42] Gong, Xing, Chen, Jiajun, Xiang, Congying, Yu, Zhiyang, Gong, Haoran, and Yin, Yuan. "A comparative study on liquid metal embrittlement susceptibility of three FeCrAl ferritic alloys in contact with liquid lead-bismuth eutectic at 350°C". In: *Corrosion Science* 183 (2021), p. 109346. ISSN: 0010-938X. DOI: 10.1016/j.corsci.2021.109346. URL: https://www.sciencedirect.com/science/article/pii/S0010938X21001128.

[43] Dai, Y., Long, B., Jia, X., Glasbrenner, H., Samec, K., and Groeschel, F. "Tensile tests and TEM investigations on LiSoR-2 to -4". In: *Journal of Nuclear Materials* 356.1 (2006). Proceedings of the Seventh International Workshop on Spallation Materials Technology, pp. 256–263. ISSN: 0022-3115. DOI: 10.1016/j.jnucmat.2006.05.010. URL: https://www.sciencedirect.com/science/article/pii/S0022311506002674.

[44] Long, B., Dai, Y., and Baluc, N. "Investigation of liquid LBE embrittlement effects on irradiated ferritic/martensitic steels by slow-strain-rate tensile tests". In: *Journal of Nuclear Materials* 431.1 (2012). Special Issue of the Tenth International Workshop on Spallation Materials Technology, (IWSMT-10), pp. 85–90. ISSN: 0022-3115. DOI: 10.1016/j.jnucmat.2011.11.036. URL: https://www.sciencedirect.com/science/article/pii/S0022311511009913.

[45] Konstantinović, M.J., Stergar, E., Lambrecht, M., and Gavrilov, S. “Comparison of the mechanical properties of T91 steel from the MEGAPIE, and TWIN-ASTIR irradiation programs”. In: *Journal of Nuclear Materials* 468 (2016), pp. 228–231. ISSN: 0022-3115. DOI: 10.1016/j.jnucmat.2015.07.038. URL: https://www.sciencedirect.com/science/article/pii/S0022311515301252.

[46] Agarwal, S., Lin, Y., Li, C., Stoller, R.E., and Zinkle, S.J. “On the use of SRIM for calculating vacancy production: Quick calculation and full-cascade options.” In: *Nuclear Instruments and Methods in Physics Research Section B: Beam Interactions with Materials and Atoms* 503 (2021), pp. 11–29. ISSN: 0168-583X. DOI: 10.1016/j.nimb.2021.06.018.

[47] James F. Ziegler Jochen P. Biersack, Matthias D. Ziegler. *SRIM The Stopping and Range of Ions in Matter*. 2008. ISBN: 9780965420716.

[48] Stoller, R.E., Toloczko, M.B., Was, G.S., Certain, A.G., Dwaraknath, S., and Garner, F.A. “On the use of SRIM for computing radiation damage exposure”. In: *Nuclear Instruments and Methods in Physics Research Section B: Beam Interactions with Materials and Atoms* 310 (2013), pp. 75–80. ISSN: 0168-583X. DOI: 10.1016/j.nimb.2013.05.008. URL: https://www.sciencedirect.com/science/article/pii/S0168583X13005053.

[49] Agarwal, S., Lin, Y., Li, C., Stoller, R.E., and Zinkle, S.J. “On the use of SRIM for calculating vacancy production: Quick calculation and full-cascade options”. In: *Nuclear Instruments and Methods in Physics Research Section B: Beam Interactions with Materials and Atoms* 503 (2021), pp. 11–19. ISSN: 0168-583X. DOI: 10.1016/j.nimb.2021.06.018. URL: https://www.sciencedirect.com/science/article/pii/S0168583X21002299.

[50] *Thomson. Precision Linear Actuators*. Accessed: 2023-05-22. URL: https://www.thomsonlinear.com/en/products/precision-linear-actuators/pc-series.

[51] Field, Kevin G., Briggs, Samuel A., Edmondson, Philip D., Haley, Jack C., Howard, Richard H., Hu, Xunxiang, Littrell, Kenneth C., Parish, Chad M., and Yamamoto, Yukinori. *Database on Performance of Neutron Irradiated FeCrAl Alloys*. Oak Ridge National Laboratory, 2016. eprint: https://info.ornl.gov/sites/publications/files/Pub68773.pdf.

[52] Airiskallio, E., Nurmi, E., Heinonen, M. H., Väyrynen, I. J., Kokko, K., Ropo, M., Punkkinen, M. P. J., Pitkänen, H., Alatalo, M., Kollár, J., Johansson, B., and Vitos, L. “Third element effect in the surface zone of Fe-Cr-Al alloys”. In: *Phys. Rev. B* 81 (3 Jan. 2010), p. 033105. DOI: 10.1103/PhysRevB.81.033105. URL: https://link.aps.org/doi/10.1103/PhysRevB.81.033105.